

Spherical deconvolution of multichannel diffusion MRI data with non-Gaussian noise models and total variation spatial regularization

Erick J. Canales-Rodríguez^{1,2,§}, Alessandro Daducci^{3,4*}, Stamatios N. Sotiropoulos^{5*}, Emmanuel Caruyer⁶, Santiago Aja-Fernández⁷, Joaquim Radua^{1,8}, Yosu Yurramendi Mendizabal⁹, Yasser Iturria-Medina¹⁰, Lester Melie-García¹¹, Yasser Alemán-Gómez^{2,12,13}, Jean-Philippe Thiran^{3,4}, Salvador Sarró^{1,2}, Edith Pomarol-Clotet^{1,2}, Raymond Salvador^{1,2}.

Erick Jorge Canales-Rodríguez ([§]**Corresponding author**, e-mail: ejcanalesr@gmail.com)

* These authors contributed equally to this work

¹ FIDMAG Germanes Hospitalàries, C/ Dr. Antoni Pujadas, 38, 08830, Sant Boi de Llobregat, Barcelona, Spain. Tel: +34 93 6529999, Fax: +34 936400268.

² Centro de Investigación Biomédica en Red de Salud Mental, CIBERSAM, C/Dr Esquerdo, 46, 28007, Madrid, Spain.

³ Signal Processing Lab (LTS5), École polytechnique fédérale de Lausanne (EPFL), Switzerland.

⁴ University Hospital Center (CHUV) and University of Lausanne (UNIL), Switzerland.

⁵ Centre for Functional Magnetic Resonance Imaging of the Brain (FMRIB), University of Oxford, John Radcliffe Hospital, Oxford OX39DU, United Kingdom.

⁶ Section of Biomedical Image Analysis, Department of Radiology, University of Pennsylvania, USA.

⁷ Laboratorio de Procesado de Imagen (LPI), ETSI Telecomunicación, Universidad de Valladolid, Valladolid, Spain.

⁸ Institute of Psychiatry, King's College London, London, United Kingdom.

⁹ Departamento de Ciencias de la Computación e Inteligencia Artificial, Universidad del País Vasco - Euskal Herriko Unibertsitatea.

¹⁰ McConnell Brain Imaging Center, Montreal Neurological Institute, McGill University, Montreal, Quebec, Canada.

¹¹ The Neuroimaging Research Laboratory (Laboratoire de Recherche en Neuroimagerie: LREN), Department of Clinical Neurosciences, University Hospital Center (CHUV), Lausanne, Switzerland.

¹² Departamento de Bioingeniería e Ingeniería Aeroespacial. Universidad Carlos III de Madrid.

¹³ Instituto de Investigación Sanitaria Gregorio Marañón. Madrid.

ABSTRACT

Due to a higher capability in resolving white matter fiber crossings, Spherical Deconvolution (SD) methods have become very popular in brain fiber-tracking applications. However, while some of these estimation algorithms assume a central Gaussian distribution for the MRI noise, its real distribution is known to be non-Gaussian and to depend on many factors such as the number of coils and the methodology used to combine multichannel signals. Indeed, the two prevailing methods for multichannel signal combination lead to noise patterns better described by Rician and noncentral Chi distributions. Here we develop a Robust and Unbiased Model-BAsed Spherical Deconvolution (RUMBA-SD) technique intended to deal with realistic MRI noise. The algorithm relies on a maximum a posteriori formulation based on Rician and noncentral Chi likelihood models and includes a total variation (TV) spatial regularization term. By means of a synthetic phantom contaminated with noise mimicking patterns generated by data processing in multichannel scanners, the performance of RUMBA-SD is compared to that of other well-established SD methods (i.e., CSD and dRL-SD). The inclusion of proper likelihood models and TV regularization in RUMBA-SD leads to an increased ability to resolve fiber crossings with smaller inter-fiber angles and an increased robustness to noise. Finally, the proposed method is also validated in human brain data, producing the most stable fiber reconstructions in front of differing noise types and diffusion schemes based on a small number of gradient directions.

Keywords: diffusion weighted imaging; spherical deconvolution; Rician noise; noncentral Chi noise; total variation.

1. INTRODUCTION

After decades of developments in diffusion Magnetic Resonance Imaging (MRI), the successful implementation of a variety of advanced methods has shed light on the complex patterns of brain organization present at micro (Salat et al., 2005) and macroscopic scales (Hagmann et al., 2008; Iturria-Medina et al., 2011; Iturria-Medina et al., 2008). Among these methods, Diffusion Tensor Imaging (DTI) (Basser et al., 1994) has become a classic in both clinical and research studies. DTI can deliver quantitative results, it may be easily implemented in any clinical MRI system and, thanks to its short acquisition time, it may be suitable for studying a wide range of brain diseases. Unfortunately, it is now well recognized that due to its simplistic assumptions, including Gaussian diffusion, the DTI model does not adequately describe diffusion processes in areas of complex tissue organization (e.g. areas with kissing, branching or crossing fibers) (Tuch et al., 2002).

Such limitations in the DTI approach have prompted the recent development of numerous sampling protocols, diffusion models and reconstruction techniques (Assemlal et al., 2011; Daducci et al., 2014a; Fillard et al., 2011). While some of these techniques have been based on model-free methods, including q-ball imaging (Tuch, 2004) and its extensions (Aganj et al., 2010; Anderson, 2005; Canales-Rodríguez et al., 2009; Descoteaux et al., 2007; Hess et al., 2006; Tristan-Vega et al., 2009, 2010), diffusion orientation transforms (Canales-Rodríguez et al., 2010b; Ozarslan et al., 2006), diffusion spectrum imaging (Wedeen et al., 2005) and related q-space techniques (Canales-Rodríguez et al., 2010a; Descoteaux et al., 2011; Hosseinbor et al., 2013; Wu and Alexander, 2007; Yeh et al., 2010), other approaches have relied on parametric diffusion models using higher-order tensors (Jensen et al., 2005; Liu et al., 2004; Ozarslan and Mareci, 2003) and multiple second-order diffusion tensors (Tuch et al., 2002). In the later group, different numerical techniques involving gradient descent (Tuch et al., 2002), Bayesian inference (Behrens et al., 2007; Jbabdi et al., 2012; Melie-Garcia et al., 2008) and algorithms inspired from compressed sensing theory (Daducci et al., 2014c; Landman et al., 2012; Michailovich et al., 2011) have been applied to obtain parameters of interest.

Spherical Deconvolution (SD) is a class of multi-compartment reconstruction technique that can be implemented using both parametric and nonparametric signal models (Alexander, 2005; Behrens et al., 2003; Dell'Acqua et al., 2007; Dell'acqua et al., 2010; Descoteaux et al., 2009; Jian and Vemuri, 2007; Kaden et al., 2007; Kaden and Kruggel, 2012; Patel et al., 2010; Ramirez-Manzanares et al., 2007; Sotiropoulos et al., 2012; Tournier et al., 2007; Tournier et al., 2004). SD methods have become very popular owing to their ability to resolve fiber crossings with small inter-fiber angles in datasets acquired within a clinically feasible scan time. This resolving power is driven by the fact that, as opposed to model-free techniques which estimate the diffusion Orientational Distribution Function (ODF), the output from SD is directly the fiber ODF itself.

Among the different SD algorithms, Constrained Spherical Deconvolution (CSD) (Tournier et al., 2007; Tournier et al., 2004) has been received with special interest due to its good performance and short computational time. In CSD, the average signal profile from white-matter regions of parallel fibers is first estimated, and afterwards, the fiber ODF is estimated by deconvolving the measured diffusion data in each voxel with this signal profile (which is also known as the single-fiber ‘response function’).

More recently and as an alternative to CSD, a new robust model-based SD method has been proposed. This method is based on a damped Richardson-Lucy algorithm adapted to Gaussian noise (dRL-SD) (Dell'Acqua et al., 2007; Dell'acqua et al., 2010). An extensive evaluation of both CSD and dRL-SD algorithms has revealed a superior ability to resolve low anisotropy crossing-fibers by CSD but a lower percentage of spurious fiber orientations and a lower over-all sensitivity to the selection of the response function by the dRL-SD approach (Parker et al., 2013). This later feature is of great relevance since the assumption of a common response function for all brain tracts is a clear over-simplification of both methods, with the consequences of it minimized by the dRL-SD.

From an algorithmic perspective dRL-SD inherits the benefits of the standard RL deconvolution method applied with great success in diverse fields ranging from microscopy (Dey et al., 2006) to astronomy (Starck et al., 2002). Remarkably, RL deconvolution is robust to the experimental

noise and the obtained solution can be constrained to be non-negative without the need for including additional penalization functions in the estimation process. Moreover, from a modeling point of view, dRL-SD is implemented using an extended multi-compartment model that allows considering the partial volume effect in brain voxels with mixture of white matter (WM), gray matter (GM) and cerebrospinal fluid (CSF), a strategy that has been shown to be effective in reducing the occurrence of spurious fiber orientations (Dell'acqua et al., 2010).

However, in spite of the good properties of dRL-SD and other SD methods some methodological issues remain. Both dRL-SD and CSD, to some extent, assume additivity and zero mean Gaussianity for the underlying noise and are potentially vulnerable to significant departures from such an assumption. Indeed, it is well known that the MRI noise is non-Gaussian and depends on many factors, including the number of coils and the multichannel image combination method. Real experiments have shown that noise follows Rician (Gudbjartsson and Patz, 1995) and noncentral Chi ($nc-\chi$) distributions (Dietrich et al., 2008) evidencing the inappropriateness of the Gaussian model. This issue is especially relevant in diffusion MRI where high b-values required to enhance the angular contrast lead to extremely low signal-to-noise (SNR) ratios. Also, a recent study (Sotiropoulos et al., 2013) has shown that different multichannel image combination methods can change the properties of the signal and can have an effect on fiber orientation estimation.

On the other hand, the standard reconstruction in SD, based on a voxel-by-voxel fiber ODF estimation, although reasonable it may not be optimal in a global sense as it does not take into account the underlying spatial continuity of the image. Recent research on the inclusion of spatial continuity into SD methods via regularization has yielded promising results (Daducci et al., 2014a; Reisert and Kiselev, 2011; Tournier et al., 2013). Among these, spatially regularized SD methods based on Total Variation (TV) (Daducci et al., 2014a) are very appealing due to their outstanding ability to simultaneously smooth away noise in flat regions whilst preserving edges, and due to their robustness to high levels of noise (Rudin et al., 1992).

The main contribution of our study is the development of a unified SD estimation framework which, following a more realistic view, deals with both Rician and $nc-\chi$ noise distributions. The

estimation algorithm proposed relies on a maximum a posteriori formulation based on Rician and $nc\text{-}\chi$ likelihood models and includes a total variation (TV) spatial regularization term. As initial hypotheses we expect: (1) that the adequate modelling of the noise distribution will improve the characterization of the underlying signals, which in turn, will lead to robust and unbiased fiber ODF estimates in fiber-crossing regions, and (2) that the inclusion of the TV spatial regularization will be highly beneficial, especially in corrupted datasets with low signal-to-noise (SNR) ratios.

To test these hypotheses and to compare the relative performance against the dRL-SD and CSD methods, the different algorithms were applied to datasets generated from a synthetic phantom which had been contaminated with noise patterns mimicking the Rician and $nc\text{-}\chi$ noise distributions produced in multichannel scanners. To the best of our knowledge, this is the first evaluation of such methods in a scenario where Rician and $nc\text{-}\chi$ noise are explicitly created as a function of the number of coils, their spatial sensitivity maps, the correlation between coils, and the reconstruction methodology used to combine the multichannel signals. As a final analysis, the new method is also applied to real multichannel diffusion MRI data from a healthy subject.

Following this introduction there is a ‘Theory’ section providing an overview of the different topics relevant to the study and the derivation of the new SD reconstruction algorithm. Description about computer simulations, image acquisition strategies and metrics designed to evaluate the performance of the reconstructions is provided in the Materials and Methods section. Relevant findings are succinctly described in the Results section. Finally, main results, contributions and limitations of this work are addressed in the Discussion and Conclusions section.

2. THEORY

This section contains a description of the local forward/generative model used to relate the local diffusion process with the measured diffusion MRI data. It also provides a brief review of MRI noise models. Finally, the diffusion and MRI noise models are used to derive the new general SD reconstruction algorithm.

2.1 Generative signal and fiber ODF model

The diffusion MRI signal measured for a given voxel can be expressed as the sum of the signals from each intra-voxel compartment. The term ‘compartment’ is defined as a homogeneous region in which the diffusion process possesses identical properties in magnitude and orientation throughout, and which is different to the diffusion processes occurring in other compartments. One example of this approach is the multi-tensor model that allows considering multiple WM parallel-fiber populations within the voxel. In this model the diffusion process taking place inside each compartment of parallel fibers is described by a second-order self-diffusion tensor (Tuch et al., 2002).

In real brain data, in addition to the different WM compartments, voxels might also contain GM and CSF components. This issue was considered by (Dell'acqua et al., 2010), who extended the multi-tensor model by incorporating the possible contribution from these compartments. This is the generative multi-tissue signal model that will be used in the present study. In the absence of any source of noise, the resulting expression for the signal is:

$$S_i = S_0 \left(\sum_{j=1}^M f_j \exp(-b_i \mathbf{v}_i^T \mathbf{D}_j \mathbf{v}_i) + f_{GM} \exp(-b_i D_{GM}) + f_{CSF} \exp(-b_i D_{CSF}) \right), \quad (1)$$

where M is the total number of WM parallel fiber bundles; f_j denotes the volume fraction of the j th fiber-bundle compartment; f_{GM} and f_{CSF} are the volume fractions of the GM and CSF

compartments respectively, so that $\sum_{j=1}^M f_j + f_{GM} + f_{CSF} = 1$; b_i is the diffusion-sensitization factor (i.e., b -value) used in the acquisition scheme to measure the diffusion signal S_i along the diffusion-sensitizing gradient unit vector \mathbf{v}_i , $i=1, \dots, N$; D_{GM} and D_{CSF} are respectively the mean diffusivity coefficients in GM and CSF; S_0 is the signal amplitude in the absence of diffusion-sensitization gradients ($b_i = 0$); $\mathbf{D}_j = \mathbf{R}_j^T \mathbf{A} \mathbf{R}_j$ denotes the anisotropic diffusion tensor of the j th fiber-bundle, where \mathbf{R}_j is the rotation matrix that rotates a unit vector initially oriented along the x-axis toward the j th fiber orientation (θ_j, ϕ_j) and \mathbf{A} is a diagonal matrix containing information about the magnitude and anisotropy of the diffusion process inside that compartment:

$$\mathbf{A} = \begin{pmatrix} \lambda_1 & 0 & 0 \\ 0 & \lambda_2 & 0 \\ 0 & 0 & \lambda_3 \end{pmatrix}, \quad (2)$$

where λ_1 is the diffusivity along the j th fiber orientation, λ_2 and λ_3 are the diffusivities in the plane perpendicular to it. It is assumed that $\lambda_1 > \lambda_2 \approx \lambda_3$.

At each voxel, the measured diffusion signals S_i for N different sampling parameters (i.e., \mathbf{v}_i and b_i , $i \in [1, \dots, N]$) can be recast in matrix form as:

$$\mathbf{S} = \mathbf{H} \mathbf{f}, \quad (3)$$

where $\mathbf{S} = [S_1 \ \dots \ S_i \ \dots \ S_N]^T$ and $\mathbf{H} = [\mathbf{H}^{WM} \ | \ \mathbf{H}^{ISO}]$ comprises two sub-matrices. \mathbf{H}^{WM} is an $N \times M$ matrix where every column of length N contains the values of the signal generated by the model given in Eq. (1) for a single fiber-bundle compartment oriented along one of the M -

directions, i.e., the (i, j) th element of \mathbf{H}^{WM} is equal to $\mathbf{H}_{ij}^{WM} = S_0 \exp(-b_i \mathbf{v}_i^T \mathbf{D}_j \mathbf{v}_i)$. Likewise, \mathbf{H}^{ISO} is an $N \times 2$ matrix where each of the two columns of length N contains the values of the signal for each isotropic compartment, i.e., $\mathbf{H}_{i1}^{ISO} = S_0 \exp(-b_i D_{GM})$ and $\mathbf{H}_{i2}^{ISO} = S_0 \exp(-b_i D_{CSF})$. Finally, the column-vector \mathbf{f} of length $M+2$ includes the volume fractions of each compartment of the voxel.

In the framework of model-based spherical deconvolution, \mathbf{H} is created by specifying the diffusivities, which are chosen according to prior information, and by providing a dense discrete set of equidistant M -orientations $\Omega = \{(\theta_j, \phi_j), j \in [1, \dots, M]\}$ uniformly distributed on the unit sphere. Previous studies have used different sets of orientations, ranging from $M=129$ (Ramirez-Manzanas et al., 2007) to $M=752$ (Dell'Acqua et al., 2007). Then, the goal is to infer the magnitude of each predefined oriented fiber, \mathbf{f} , from the vector of measurements \mathbf{S} and the ‘dictionary’ \mathbf{H} of oriented basis signals. Under this reconstruction model, \mathbf{f} can be interpreted to as the fiber ODF evaluated on the set Ω . Matrix \mathbf{H} is referred to in other contexts as the ‘diffusion basis functions’ (Ramirez-Manzanas et al., 2007), or the ‘point spread function’ (Dell'acqua et al., 2010; Kaden et al., 2007; Tournier et al., 2007) that blurs the fiber ODF to produce the observed measurements.

It should be noticed that solving the deconvolution problem given by Eq. (3) is not simple because the resulting system of linear equations is ill-conditioned and ill-posed (i.e., there are more unknowns than measurements and some of the columns of \mathbf{H} are highly correlated), which can lead to numerical instabilities and physically meaningless results (e.g., volume fractions with negative values). A common strategy to avoid such instabilities is to use robust algorithms that search for solutions compatible with the observed data but which also satisfy some additional constraints. Thus, in both CSD and dRL-SD the estimated fiber ODFs are constrained to be non-negative and symmetric around the origin (i.e., antipodal symmetry). The stability of CSD is further increased by assuming that the fiber ODF is a smooth function on the sphere. Compliance with this assumption is achieved by representing the fiber ODF in terms of spherical harmonic basis with a low number of terms, thus reducing the dimensionality of the problem. On the other

hand, in contrast to standard estimation algorithms, the dRL-SD implementation does not involve any matrix inversion, which is crucial to avoid the instability that arises when inverting the resulting dictionary \mathbf{H} . As mentioned in the introduction, though, all these reconstruction algorithms may not be necessarily optimal when dealing with non-Gaussian noise, as it is the case for MRI noise.

2.2 MRI noise models

In conventional MRI systems, the data are measured using a single quadrature detector (i.e., coil with two orthogonal elements) that gives two signals which, for convenience, are treated as the real and imaginary parts of a complex number. The magnitude of this complex number (i.e. the square root of the sum of their squares) is commonly used because it avoids different kinds of MRI artifacts (Gudbjartsson and Patz, 1995). Given that the noise in the real and imaginary components follows a Gaussian distribution, the magnitude signal S_i will follow a Rician distribution (Gudbjartsson and Patz, 1995) with a probability function given by

$$P(S_i | \bar{S}_i, \sigma^2) = \frac{S_i}{\sigma^2} \exp\left\{-\frac{1}{2\sigma^2}[S_i^2 + \bar{S}_i^2]\right\} I_0\left(\frac{S_i \bar{S}_i}{\sigma^2}\right) u(S_i), \quad (4)$$

where \bar{S}_i denotes the true magnitude signal intensity in the absence of noise, σ^2 is the variance of the Gaussian noise in the real and imaginary components, I_0 is the modified Bessel function of first kind of order zero and u is the Heaviside step function that is equal to 0 for negative arguments and to 1 for non-negative arguments.

Modern clinical scanners are usually equipped with a set of 4 to 32 multiple phased-array coils, the signals of which can be combined following different strategies that, in turn, will give rise to different statistical properties for the noise (Dietrich et al., 2008). One frequent strategy uses the spatial matched filter (SMF) approach linearly combining the complex signals of each coil and producing voxelwise complex signals (Blaimer et al., 2004). Since the noise in the resulting real

and imaginary components remains Gaussian a Rician distribution is expected in the final combined magnitude image. An alternative to the SMF is to create the composite magnitude image as the root of the sum-of-squares (SoS) of the complex signals of each coil. Under this approach the combined image follows a nc- χ distribution (Constantinides et al., 1997) given by,

$$P(S_i | \bar{S}_i, \sigma^2, n) = \frac{\bar{S}_i}{\sigma^2} \left(\frac{S_i}{\bar{S}_i} \right)^n \exp \left\{ -\frac{1}{2\sigma^2} [S_i^2 + \bar{S}_i^2] \right\} I_{n-1} \left(\frac{S_i \bar{S}_i}{\sigma^2} \right) u(S_i), \quad (5)$$

where n is the number of coils and I_{n-1} is the modified Bessel function of first kind of order $n-1$. This expression is strictly valid when the different coils have equal variance and uncorrelated noise, and when noise correlation cannot be neglected it provides a good approximation if effective n_{eff} and σ_{eff}^2 values are considered (Aja-Fernandez et al., 2011), with n_{eff} being a non-integer number lower than the real number of coils and σ_{eff}^2 is higher than the real noise variance in each coil.

A related SoS image combination method that increases the validity of Eq. (5) is the covariance-weighted SoS. This method is equivalent to pre-whitening (i.e., decorrelate) the measured signals before applying the standard SoS image combination. The covariance-weighted SoS approach requires the estimation of the noise covariance matrix of the system which, in practice, may be carried out by digitizing noise from the coils in the absence of excitations (Keil and Wald, 2013).

It is important to note that there are additional factors that can change the noise characteristics described above, including the use of accelerated techniques such as parallel MRI (pMRI) and partial Fourier, certain reconstruction filters in k-space, and some of the preprocessing steps conducted after image reconstruction.

Empirical data suggest that some of these factors do not substantially change the type of distribution of the noise. On the one hand, (Dietrich et al., 2008) investigated the effects of the type of filter in k-space, the number of receiving channels and the use of pMRI reconstruction

techniques, and found that noise distributions always followed Rician and nc- χ distributions with a reasonable accuracy - although their standard deviations and effective number of receiver channels were altered when fast pMRI and subsequent SoS reconstructions were used. On the other hand, (Sotiropoulos et al., 2013) showed real diffusion MRI data noise to also follow Rician and nc- χ noise distributions after a preprocessing that included motion and eddy currents corrections. Unfortunately, the combined effect of all factors has not, to the best of our knowledge, been studied. In this regard, a complete evaluation should include the study of the effects of additional data manipulation processes routinely applied in many clinical research studies, such as B0-unwarping due to magnetic field inhomogeneity and partial Fourier reconstructions. Although the latter has been investigated in terms of signal-to-noise ratio, its influence on the shape of the noise distribution remains unknown.

However, while it is impossible to ensure that Rician and nc- χ distributions are the optimal noise models for all possible strategies used for sampling, reconstructing and preprocessing diffusion MRI data, such models are flexible enough to adapt to deviations from the initial theoretical assumptions via re-parameterization in terms of spatial-dependent effective parameters (i.e., $n_{eff}(x, y, z)$, $\sigma_{eff}^2(x, y, z)$), as in (Aja-Fernandez and Tristan-Vega, 2012; Aja-Fernandez et al., 2011; Aja-Fernandez et al., 2014). Moreover, the use of effective parameters allows characterizing the spatially varying nature of the noise in accelerated MRI reconstructed data, as well as the additional spatial correlation introduced by reconstruction algorithms, whilst preserving the good theoretical properties of the models with standard parameters (i.e. the null probability to obtain negative signals as expected from magnitude MRI data, and the ability to characterize the signal-dependent non-linear bias of the data).

2.3 Spherical deconvolution of diffusion MRI data

Equation (5) based on either conventional (i.e., n , σ^2) or effective (i.e., n_{eff} , σ_{eff}^2) parameters provides a very general MRI noise model, which includes the Rician distribution (given in Eq. (4)) as a special case with $n=1$. Consequently, if we derive the spherical deconvolution

reconstruction corresponding to Equation (6) any particular solution of interest will become available.

Specifically, if we assume the linear model given by Eqs. (1)-(3) the likelihood model for the vector of measurements \mathbf{S} under a nc- χ distribution is

$$P(\mathbf{S}|\mathbf{H}, \mathbf{f}, \sigma^2, n) = \prod_{i=1}^N \frac{\bar{S}_i}{\sigma^2} \left(\frac{S_i}{\bar{S}_i} \right)^n \exp \left\{ -\frac{1}{2\sigma^2} [S_i^2 + \bar{S}_i^2] \right\} I_{n-1} \left(\frac{S_i \bar{S}_i}{\sigma^2} \right) u(S_i), \quad (6)$$

where S_i and $\bar{S}_i = (\mathbf{H}\mathbf{f})_i$ are the measured and expected signal intensities for i th sampling parameters, respectively.

2.3.1 Unbiased and positive recovery: the multiplicative Richardson-Lucy algorithm for nc- χ noise

The maximum likelihood (ML) estimate in Eq. (6) is obtained by differentiating its negative log-likelihood $J(\mathbf{f}) = -\log P(\mathbf{S}|\mathbf{H}, \mathbf{f}, \sigma^2, n)$ with respect to \mathbf{f} and equating the derivative to zero, which after some algebraic manipulations becomes

$$\mathbf{f} = \mathbf{f} \circ \frac{\mathbf{H}^T \left[\mathbf{S} \circ \frac{I_n(\mathbf{S} \circ \mathbf{H}\mathbf{f}/\sigma^2)}{I_{n-1}(\mathbf{S} \circ \mathbf{H}\mathbf{f}/\sigma^2)} \right]}{\mathbf{H}^T \mathbf{H}\mathbf{f}}, \quad (7)$$

where ‘ \circ ’ stands for the Hadamard component-wise product, and the division operators are applied component-wise to the vector’s elements.

Equation (7) is nonlinear in \mathbf{f} and its solution can be obtained through a modified version of the expectation maximization technique, originally developed by Richardson and Lucy for a Poisson

noise (Lucy, 1974; Richardson, 1972) and known as the RL algorithm. When we applied this technique to nc- χ and Rician distributed noise it naturally led to the following iterative estimation formula

$$\mathbf{f}^{k+1} = \mathbf{f}^k \circ \frac{\mathbf{H}^T \left[\mathbf{S} \circ \frac{I_n(\mathbf{S} \circ \mathbf{H}\mathbf{f}^k / \sigma^2)}{I_{n-1}(\mathbf{S} \circ \mathbf{H}\mathbf{f}^k / \sigma^2)} \right]}{\mathbf{H}^T \mathbf{H}\mathbf{f}^k} \quad (8)$$

in which the solution calculated at the k th iteration step (\mathbf{f}^k) gradually improves (i.e. its likelihood increases after each step) until a final, stationary solution, is reached. As shown in Appendix A this formula can also be related to the RL algorithm for Gaussian noise, employed in the undamped RL-SD technique (Dell'Acqua et al., 2007).

Under the absence of any prior knowledge about \mathbf{f} , the initial estimate (\mathbf{f}^0) can be fixed to a non-negative constant density distribution (Dell'Acqua et al., 2007). In that case, the algorithm transforms a perfectly smooth initial estimate into sharper estimates, with sharpness increasing with the number of iterations. So, roughly speaking, the number of iterations can be considered as a regularization parameter controlling the angular smoothness of the final estimate. Notably, if \mathbf{f}^0 is non-negative, the successive estimates remain non-negative as well, and the algorithm always produces reconstructions with positive elements. Moreover, as in (Dell'Acqua et al., 2007; Dell'acqua et al., 2010) the estimation does not involve any matrix inversion, thus avoiding related numerical instabilities.

In order to evaluate Eq. (8) an estimate $\tilde{\sigma}^2$ of σ^2 is required. Although obtaining it from a region-of-interest (ROI) is feasible (Henkelman, 1985) its accuracy may be compromised by systematic experimental issues such as ghosting artifacts, signal suppression by the scanner outside the brain, zero-padding and by filters applied in the k -space. Moreover, with the use of fast parallel MRI sequences, where each coil records signals with partial coverage in the k -space, properties of the noise become spatially heterogeneous (i.e. they change from voxel to voxel across the image). While some authors have proposed alternatives to overcome this limitation

(Aja-Fernandez et al., 2009) here we have estimated the noise variance at each voxel from the same data used to infer the fiber ODF.

Specifically, by minimizing the negative log-likelihood with respect to σ^2 we have obtained an iterative scheme analogous to Eq. (9):

$$\alpha^{k+1} = \frac{1}{nN} \left\{ \frac{\mathbf{S}^T \mathbf{S} + \mathbf{f}^T \mathbf{H}^T \mathbf{H} \mathbf{f}}{2} - \mathbf{1}_N^T \left[(\mathbf{S} \circ \mathbf{H} \mathbf{f}) \circ \frac{I_n(\mathbf{S} \circ \mathbf{H} \mathbf{f} / \alpha^k)}{I_{n-1}(\mathbf{S} \circ \mathbf{H} \mathbf{f} / \alpha^k)} \right] \right\}, \quad (9)$$

where α^k is the estimate of σ^2 at the k th iteration (starting with an arbitrarily initial estimate α^0) and $\mathbf{1}_N$ is a $N \times 1$ vector of ones. In summary, equations (8) and (9) provide the basic ingredients for inference. However, the final version of our algorithm includes a spatially regularized extension, which is described in the following section.

2.3.2 Towards a robust recovery: Total variation regularization

When considering the TV model (Rudin et al., 1992) the maximum a posteriori (MAP) solution at voxel (x, y, z) is obtained by minimizing the augmented functional:

$$J(\mathbf{f}) = -\log P(\mathbf{S} | \mathbf{H}, \mathbf{f}, \sigma^2, n) + \alpha_{TV} \sum_j |\nabla[\mathbf{f}]_j|, \quad (10)$$

where the first term is the negative log-likelihood defined in previous sections and the second term is the TV energy evaluated at voxel (x, y, z) . $[\mathbf{f}]_j$ is a 3D image created in a way that each voxel contains the element at position j of their corresponding estimate vector \mathbf{f} , and α_{TV} is a parameter controlling the level of spatial regularization. Importantly, and in contrast to the

previous ML estimate, now the solution at a given voxel is not independent from the solutions in other voxels. The spatial dependence introduced by the TV functional promote solutions that minimize the sum of the absolute values of the first-order spatial derivative (i.e., gradient “ ∇ ”) of the fiber ODF components over the entire brain image. This means that, although TV regularization does penalize oscillations in homogeneous regions, it does not penalize discontinuities (Rudin et al., 1992). This property is highly relevant for SD because, while it promotes continuity and smoothness along individual tracts, it prevents partial volume contamination from adjacent tracts.

MAP estimates are obtained by differentiating the functional in Eq.(10) with respect to \mathbf{f} and equating the derivative to zero. This yields the following iterative formula (see (Dey et al., 2006) for a related derivation):

$$\mathbf{f}^{k+1} = \mathbf{f}^k \circ \frac{\mathbf{H}^T \left[\mathbf{S} \circ \frac{I_n(\mathbf{S} \circ \mathbf{H}\mathbf{f}^k / \sigma^2)}{I_{n-1}(\mathbf{S} \circ \mathbf{H}\mathbf{f}^k / \sigma^2)} \right]}{\mathbf{H}^T \mathbf{H}\mathbf{f}^k} \circ \mathbf{R}^k, \quad (11)$$

with the TV regularization vector \mathbf{R}^k at voxel (x, y, z) , and at the k th iteration, computed element-by-element as

$$\left(\mathbf{R}^k\right)_j = \frac{1}{1 - \alpha_{TV} \operatorname{div} \left(\frac{\nabla[\mathbf{f}^k]_j}{|\nabla[\mathbf{f}^k]_j|} \right)} \Bigg|_{(x,y,z)}, \quad (12)$$

where $\left(\mathbf{R}^k\right)_j$ is the element j of vector \mathbf{R}^k and div is the divergence operator. In practice, to correct for potential singularities at $|\nabla[\mathbf{f}^k]_j| = 0$, the term $|\nabla[\mathbf{f}^k]_j|$ is replaced by its

approximated value $\sqrt{|\nabla[\mathbf{f}^k]_j|^2} + \varepsilon$, where ε is a small positive constant. Notice that by setting $\alpha_{TV} = 0$ the estimator in Eq. (11) becomes equal to the unregularized version of Eq. (8).

In the current implementation, the simultaneous estimation of all the parameters is carried out via an alternating iterative scheme, summarized in Table 1. Briefly, it maximizes the functional in Eq. (10) with respect to the fiber ODF while assuming that σ^2 is known and fixed, and then it updates the noise variance using the new fiber ODF estimate. While for SMF-based data all the equations are evaluated using $n = 1$, for SoS-based data n is fixed to the real number of coils, or to the effective value n_{eff} if provided. (But see Appendix B)

Insert Table 1 around here

Table 1. General pseudocode MAP algorithm.

<p>Initialize \mathbf{f}^0 and α^0</p> <p><i>if</i> SMF, then</p> <p style="padding-left: 2em;">$n = 1$</p> <p><i>else if</i> SoS, then</p> <p style="padding-left: 2em;">$n = \text{number of coils (or } n_{eff} \text{)}$</p> <p><i>end</i></p> <p><i>for</i> $k = 1, 2, \dots$, repeat the following steps, until a termination criterion is satisfied</p> <p style="padding-left: 2em;">compute \mathbf{f}^{k+1} via Eqs. (12) and (13), assuming $\sigma^2 = \alpha^k$</p> <p style="padding-left: 2em;">$\mathbf{f}^{k+1} = \max(0, \mathbf{f}^{k+1})$ (*)</p> <p style="padding-left: 2em;">$\mathbf{f}^{k+1} = \mathbf{f}^{k+1} / \text{sum}(\mathbf{f}^{k+1})$ (**)</p> <p style="padding-left: 2em;">compute α^{k+1} via Eqs. (10), assuming $\mathbf{f} = \mathbf{f}^{k+1}$</p> <p style="padding-left: 2em;">update α_{TV}</p> <p><i>end</i></p>
--

(*) Since small negative fibers may result from the introduction of the TV model, any spurious negative component is set to zero at each step of the algorithm. This increases the sparsity of the estimator because, once a component is set to zero, it remains zero at subsequent iterations.

(**) Optionally, the ODF vector may be normalized to unity, thus preserving the physical definition of the j th element in \mathbf{f} as the volume fraction of the j th compartment of the voxel (see Eqs. (1)-(3)).

Following the discrepancy principle, the regularization parameter α_{TV} is adaptively adjusted at each iteration. Specifically, it is selected to match the estimated variance (Chambolle, 2004) using two alternative strategies: (i) assuming a constant mean parameter over the entire brain image, $\alpha_{TV} = E\{\alpha^{k+1}\}$ (see Table 1), potentially increasing the precision and robustness of the estimator; or (ii) assuming a spatial dependent parameter, $\alpha_{TV}(x, y, z) = \alpha^{k+1}(x, y, z)$, which may be more appropriate in situations where a differential variance across the image is expected, like in accelerated pMRI based-data.

It should be remembered that the accuracy of the reconstruction for the SoS case depends on the variant used to combine the images. In this work it is assumed that the data is combined using the covariance-weighted SoS method. However, even if the available data were combined using the conventional SoS approach (i.e., without taking into account the noise correlation matrix among coil elements), the method could still provide a reasonable approximation (for more details see Appendix B).

The evaluation of the ratio of modified Bessel functions of first kind involved in the updates of Eqs. (11) and (9) is best computed by considering the ratio as a new composite function, and not by means of the simple evaluation of the ratio of the individual functions. Specifically, this ratio is computed here in terms of Perron continued fraction (Gautschi and Slavik, 1978). All the details are provided in Appendix C.

3. MATERIAL AND METHODS

3.1 Synthetic phantom data

The reconstruction algorithm proposed here was tested on the synthetic diffusion MRI phantom developed for the “HARDI Reconstruction Challenge 2013” Workshop, within the IEEE International Symposium on Biomedical Imaging (ISBI 2013). This phantom comprises a set of 27 fiber bundles with fibers of varying radii and geometry which connect different areas of a 3D image (matrix size: 50 x 50 x 50). It contains a wide range of configurations including branching, crossing and kissing fibers, together with the presence of isotropic compartments mimicking the CSF contamination effects occurring near ventricles in real brain images.

3.1.1 Signal generation

The intra-voxel diffusion MRI signal was generated using $N = 64$ sampling points on a sphere in q-space with constant $b=3000 \text{ s/mm}^2$, plus one additional image with $b=0$ (i.e., $S_0 = 1$ was assumed in all voxels). For pure GM and CSF voxels, signals were generated using two mono-exponential models: $\exp(-D_{GM}b)$ and $\exp(-D_{CSF}b)$ with $D_{GM} = 0.2 \cdot 10^{-3} \text{ mm}^2/\text{s}$ and $D_{CSF} = 1.7 \cdot 10^{-3} \text{ mm}^2/\text{s}$. In voxels belonging to single-fiber WM bundles, the signal measured along the q-space unit direction $\hat{\mathbf{q}} = \mathbf{q}/|\mathbf{q}|$ was generated by a mixture of signals from intra- and extra-axonal compartments: $f_{\text{int}}s_{\text{int}}(\mathbf{q}, \mathbf{v}, \tau, L, R) + f_{\text{ext}}s_{\text{ext}}(\hat{\mathbf{q}}, \mathbf{v}, b, \lambda_1, \lambda_2)$, where \mathbf{v} denotes the local fiber orientation. Signal from the intra-axonal compartment s_{int} was created following the theoretical model of a restricted diffusion process inside a cylinder of length $L = 5 \text{ mm}$ and radius $R = 5 \mu\text{m}$ at the diffusion time $\tau = 20.8 \text{ s}$ (Ozarslan et al., 2006; Söderman and Jönsson, 1995). The extra-axonal signal s_{ext} was generated using a diffusion tensor model with cylindrical symmetry (i.e., $\lambda_1 = 1.7 \cdot 10^{-3} \text{ mm}^2/\text{s}$, $\lambda_2 = \lambda_3 = 0.2 \cdot 10^{-3} \text{ mm}^2/\text{s}$). Mixture fractions were fixed to

$f_{\text{int}} = 0.6$ and $f_{\text{ext}} = 0.4$. The noiseless dataset can be freely downloaded from the Webpage of the site¹ as well as the ground-truth fiber orientations.

3.1.2 Multichannel noise generation

The synthetic diffusion image S was contaminated with noise mimicking the SoS and SMF strategies used in scanners in order to combine multiple-coils signals. To that aim, the noisy complex-valued image measured from the k th coil was assumed to be equal to

$$S_k = SC_k + e_k^R + ie_k^I, \quad (13)$$

where C_k is the relative sensitivity map (Pruessmann et al., 1999) of k th coil, $e_k^R \sim N(0, \Sigma)$ and $e_k^I \sim N(0, \Sigma)$ are two different Gaussian noise realizations simulating the noise in the real and imaginary components with zero-mean value and covariance matrix Σ . For simplicity Σ was assumed to be given by

$$\Sigma = \sigma^2 \begin{pmatrix} 1 & \rho & \cdots & \rho \\ \rho & 1 & \cdots & \rho \\ \vdots & \vdots & \ddots & \vdots \\ \rho & \rho & \cdots & 1 \end{pmatrix}, \quad (14)$$

where σ^2 is the noise variance of each coil and ρ indicates the correlation coefficient between any two coils.

For the SoS reconstruction, magnitude images were generated as:

¹ http://hardi.epfl.ch/static/events/2013_ISBI/

$$S_{SoS} = \sqrt{\sum_{k=1}^n |S_k|^2}, \quad (15)$$

where $|S_k|$ stands for the magnitude of S_k . Notice that Eq. (15) is the conventional SoS image combination and not the covariance-weighted variant. We have followed this approach in order to simulate the effect of any remaining residual correlation ρ present in real systems (we have assumed a $\rho = 0.05$) (Aja-Fernandez and Tristan-Vega, 2012).

In the SMF reconstruction, magnitude images were generated as:

$$S_{SMF} = \left| \sum_{k=1}^n S_k C_k \right|, \quad (16)$$

with simulated sensitivity maps depicted in Figure 1, satisfying the relationship $\sum_{k=1}^n C_k^2 = 1$, which holds in practice when the relative sensitivity maps are calculated as $C_k = |S_k| / S_{SoS}$ (Pruessmann et al., 1999). These maps have been previously used in (Aja-Fernandez et al., 2013)

Insert Figure 1 around here (1 column)

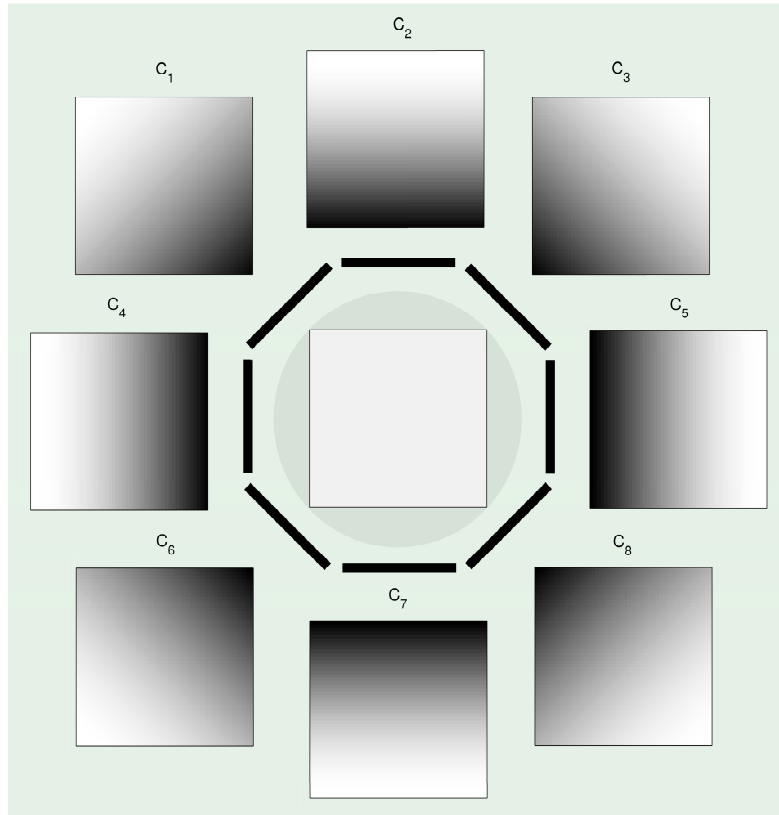


Figure 1. Sensitivity maps simulating an eight-coil system. White colors denote higher values. The constant image in the center is the sum-of-squares of the individual sensitivity maps.

It should be noted that different scanner vendors can implement different SMF and SoS variants. In this work we have used the variants given in (Sotiropoulos et al., 2013) for datasets acquired without undersampling in the k-space, i.e., $R=1$, where R is the acceleration factor of the acquisition defined as the ratio of the total k-space phase-encoding lines over the number of k-space lines actually acquired. Notice that in the absence of noise $S_{SoS} = S_{SMF}$. Besides, for the particular case of a single coil with uniform sensitivity, i.e., $n=1$ and $C=1$, Eq.(15) and Eq. (16) become identical.

Various sets of noisy signals were generated using three different values for σ , chosen to produce signal-to-noise (SNR) ratios of 10, 20 and 30 (where $SNR = S_0 / \sigma$). In order to generate signals under equivalent conditions, for each value of σ the same noise realizations $\{e_k^R\}$ and $\{e_k^I\}$ were used to generate the final images S_{SoS} and S_{SMF} . All datasets were created simulating a scanner with 8 coils (see Figure 1). Figure 2 depicts the noise distribution profiles resulting from background regions outside the phantom for the two reconstruction methods. As expected, Rician and nc- χ noise was observed in SMF and SoS, respectively.

Insert Figure 2 around here (1.5 column)

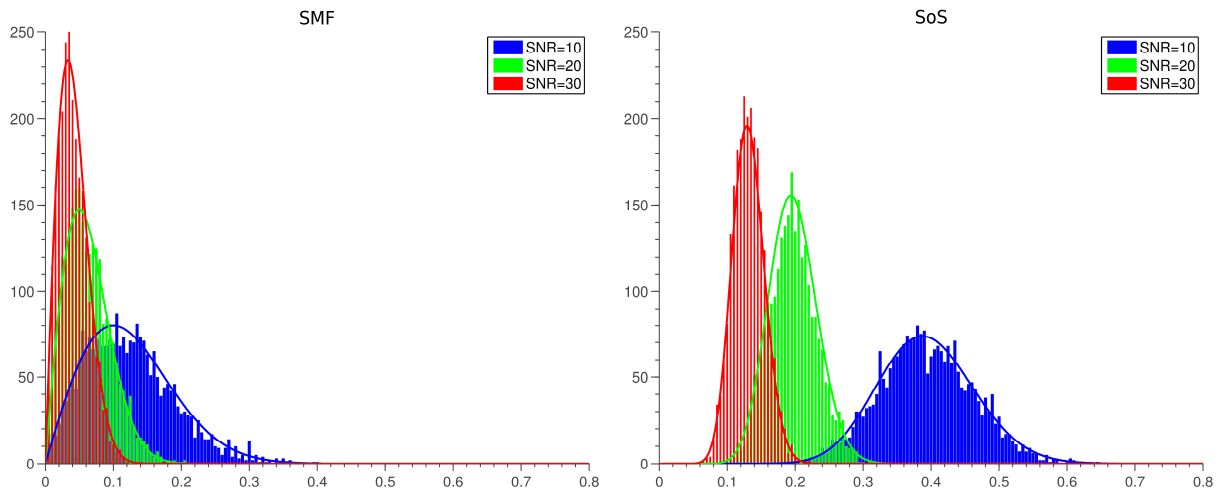


Figure 2. Noise distribution profiles resulting from background regions outside the phantom for the two reconstruction methods. Rician and noncentral Chi distributions are obtained in SMF and SoS, respectively. The mean value of the distributions increases as long as the SNR decreases. This bias is higher in the SoS data.

3.1.3 Evaluation metrics

The performance of the reconstructions was quantified by comparing the obtained reconstructions against the ground-truth via two main criteria: (i) angular error in the orientation of the fiber populations and (ii) correct estimation of the number of fiber populations present in every voxel.

For the analyses, the three main peaks from the reconstructed fiber ODFs were extracted, retaining only those with magnitude exceeding one tenth of the amplitude of the highest peak ($0.1 \cdot f_{\max}$) (Parker et al., 2013), and local peaks were identified as those vertices in the grid with higher fiber ODFs than their adjacent neighbors. Then, the angular error was defined as the average minimum angle between the extracted peaks and the true fiber directions (Canales-Rodríguez et al., 2008):

$$\bar{\theta} = \frac{1}{M_{\text{true}}} \sum_{k=1}^{M_{\text{true}}} \min_m \left\{ \arccos \left(\left| \mathbf{e}_m^T \mathbf{v}_k \right| \right) \right\}, \quad (17)$$

where M_{true} is the true number of fiber populations, \mathbf{e}_m is the unitary vector along with the m th detected fiber peak and \mathbf{v}_k is the unitary vector along the k th true fiber direction. Notice that the angular error between each pair of fibers is always measured between the true fiber and the closest estimated fiber. Hence, although this metric implicitly depends on the correct detection of the true number of fibers, it does not explicitly penalize the occurrence of spurious or undetected fibers.

To quantify any incorrect fiber detection, the mean number of over-estimated n^+ (i.e., false positive) and underestimated n^- (i.e., false negative) fiber populations over the whole image were computed (Daducci et al., 2014a). To that aim, the following procedure was adopted. Initially, all the estimated fibers forming an angle lower than 20 degrees with any of the true fibers (i.e., ground-truth) were labeled. Next, not labeled fibers were considered as spurious

fibers (n^+) and true fibers without any associated labeled fiber were considered as undetected fibers (n^-). However, since a single labeled estimated fiber could be associated to different true fibers, and differently labeled estimated fibers could be associated to a single true fiber, an update of the n^+ and n^- including such cases had to be made. In consequence, a ‘perfect’ estimation of the number of fiber populations (i.e., $n^+ = n^- = 0$) was considered only when the numbers of true and estimated fibers were equal and all estimated fibers were contained within the tolerance cone of 20 degrees around the true fibers.

3.1.4 Settings for the evaluation algorithms

RUMBA-SD estimates were compared to those from dRL-SD and CSD. To investigate the performance of the CSD as implemented in *MRtrix* software², reconstructions for all the datasets were independently computed via the *csdeconv* tool using spherical harmonic series of order $L_{\max} = 6, 8$ and 10, respectively. For each dataset, the response function was measured from the images themselves in voxels known to comprise a single bundle of parallel fibers (Tournier et al., 2008). Local peaks were obtained using the *find_SH_peaks* function, which identify the orientation of the three largest peaks from the estimated spherical harmonic coefficients, retaining only those exceeding the value $0.1 \cdot f_{\max}$ (Parker et al., 2013).

Both RUMBA-SD and dRL-SD methods were implemented using in-house *Matlab* software and the same dictionary \mathbf{H} , created from the signal generative model given in Eqs.(1)-(3). Specifically, $M = 724$ fiber orientations distributed on the unit sphere (mean angular separation between adjacent neighbor vertices/standard deviation = 8.36/1.18 degrees) were assumed, with diffusivities equal to $\lambda_1 = 1.4 \cdot 10^{-3} \text{ mm}^2/\text{s}$ and $\lambda_2 = \lambda_3 = 0.4 \cdot 10^{-3} \text{ mm}^2/\text{s}$. Two isotropic terms to account for intra- (i.e., $0.2 \cdot 10^{-3} \text{ mm}^2/\text{s}$) and extra-axonal diffusion (i.e., $1.4 \cdot 10^{-3} \text{ mm}^2/\text{s}$) were also included. The model diffusivities and the ‘true’ diffusivities in the phantom were deliberately set to different values in order to consider the possibility of model misspecification.

² <http://www.brain.org.au/software/mrtrix/>

The same dictionary was used in the estimation in both SMF- and SoS-based datasets. For SoS-based data, n was fixed to the real number of coils. The starting condition for \mathbf{f}^0 was set as a non-negative iso-probable spherical function (Dell'acqua et al., 2010). In order to investigate the accuracy and convergence of RUMBA-SD as a function of the number of iterations, various reconstructions were obtained using 200, 400, 600, 800 and 1000 iterations. In the case of dRL-SD, 200 and 400 iterations were used, which is within the optimal range as suggested in (Dell'acqua et al., 2010) and (Parker et al., 2013). The damping and threshold parameters for dRL-SD method were set to 8 and 0.06 respectively (Dell'acqua et al., 2010).

Additionally, RUMBA-SD was computed without applying the TV spatial regularization (i.e., $\alpha_{TV} = 0$) denoted hereafter as ‘RUMBA-SD without TV’ (while keeping the name ‘RUMBA-SD’ for the regularized version), and values of $\bar{\theta}$, n^+ and n^- for the standard DTI method (using the *dtifit* tool from FSL) were also calculated assuming fiber orientation through the main eigenvector. DTI results were used to evaluate the relative benefits of all other reconstruction methods.

3.2 Real brain data

Diffusion MRI data were acquired from a healthy subject on a 3T Siemens scanner (Erlangen) located at the University of Oxford (UK). The subject provided informed written consent before participating in the study, which was approved by the Institutional Review Board of the University of Oxford. Whole brain diffusion images were acquired with a 32-channel head coil along 256 different gradient directions on the sphere in q-space with constant $b = 2500 \text{ s/mm}^2$. Additionally, 36 $b = 0$ volumes were acquired with in-plane resolution = $2.0 \times 2.0 \text{ mm}^2$ and slice thickness = 2 mm. The acquisition was carried out without undersampling in the k -space (i.e., $R=1$). Raw multichannel signals were combined using either the standard GRAPPA approach or the GRAPPA approach with the adaptive combination of the SMF available in the scanner, giving SoS and SMF-based datasets respectively. Then, the two resulting datasets were

separately corrected for eddy current distortions and head motion as implemented in FSL (Smith et al., 2004).

In order to study the robustness of the methods under a lower number of measurements, subsets of 64 and 35 directions were selected from the full set of 256 gradient directions, and measurements for these subsets were used to ‘create’ two (under-sampled) versions of the data. Specifically, a k-means clustering algorithm was employed to group the 256 directions into 64 and 35 non-overlapping clusters on the sphere by selecting the gradient direction closest to each cluster centroid. This procedure allows identifying subsets of directions with nearly uniform coverage on the sphere. Finally, from the 36 acquired $b=0$ volumes only the first 3 volumes were included in the reduced datasets.

4. RESULTS

4.1 Synthetic phantom data

To differentiate the accuracy of all tested methods in regions with varying orientational complexity, the quality metrics were independently computed in single-fiber regions of parallel fibers (i.e., more than 12 000 voxels) and in multiple-fiber regions (i.e., more than 1 500 voxels with inter-fiber angles ranging from 10 to 90 degrees; mean-value/standard deviation = 50/25 degrees).

Results corresponding to single-fiber regions are show in Figure 3. A set of patterns can be drawn from these results. First, for both SMF- and SoS-based data, RUMBA-SD and dRL-SD were the methods providing the overall best metrics. Second, the performance of RUMBA-SD without TV was similar to CSD in terms of angular error and number of undetected fibers, but CSD produced a higher number of spurious fibers. Finally, all the spherical deconvolution methods produced lower angular errors than DTI.

Insert Figure 3 around here (1.5 columns)

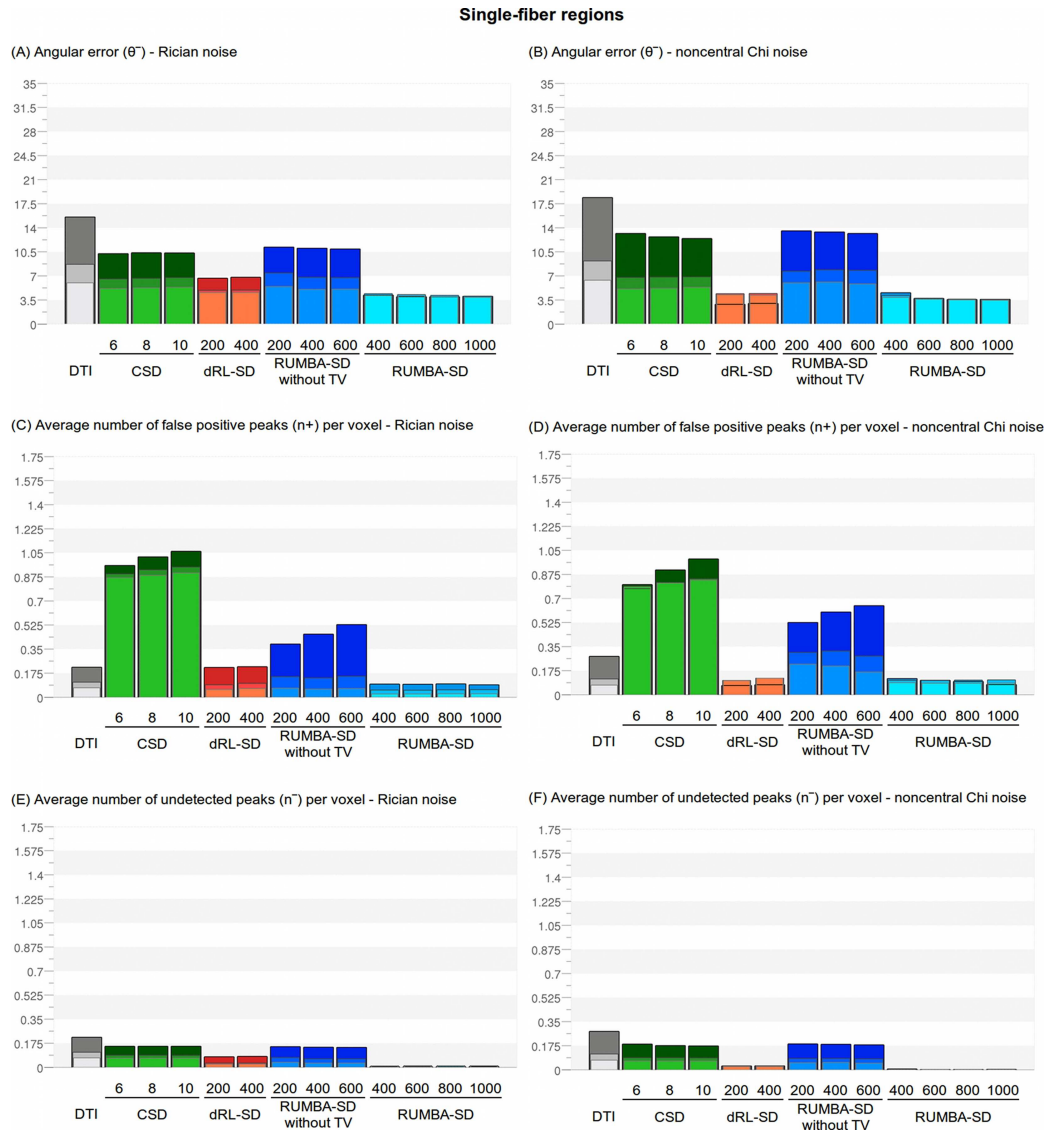


Figure 3. Quantification of the reconstruction accuracy of RUMBA-SD, RUMBA-SD without TV, dRL-SD, CSD and DTI in terms of $\bar{\theta}$ (angular error), n^+ (number of false positive) and n^- (number of false negative) in single-fiber regions of the phantom. Light colors correspond to higher SNRs.

Results from multiple-fiber regions are show in Figure 4. For both SMF- and SoS-based data, RUMBA-SD without TV and CSD performed quite similar. They performed better than dRL-SD in terms of angular error and number of undetected fibers, and worse than it in terms of number of spurious fibers. The superior ability of RUMBA-SD without TV to resolve fiber crossings, as compared to dRL-SD under the same number of algorithm iterations (i.e., 200 and 400) and dictionary of basis signals, suggest that it converges faster. RUMBA-SD was the method providing the best results in terms of all metrics studied in all SNR levels. Notably, results from RUMBA-SD at the lowest SNR (i.e., SNR = 10) were generally better than those from dRL-SD, CSD and RUMBA-SD without TV at the highest SNRs (i.e., SNR = 20 and 30); demonstrating the success of the TV regularization. The uniformity of RUMBA-SD metrics at different number of iterations suggests that the regularization increases the stability and convergence of the reconstruction. Finally, results from datasets based on SMF were better than those from SoS.

Results from DTI show a non-zero number of spurious fibers in multiple-fiber regions and existing undetected fibers in single-fiber regions. These results may seem counterintuitive, however, it should be noticed that these non-zero values are obtained due to the tolerance cone used in the experiments to classify the fibers as true positives, false positives and false negatives.

Insert Figure 4 around here (1.5 columns)

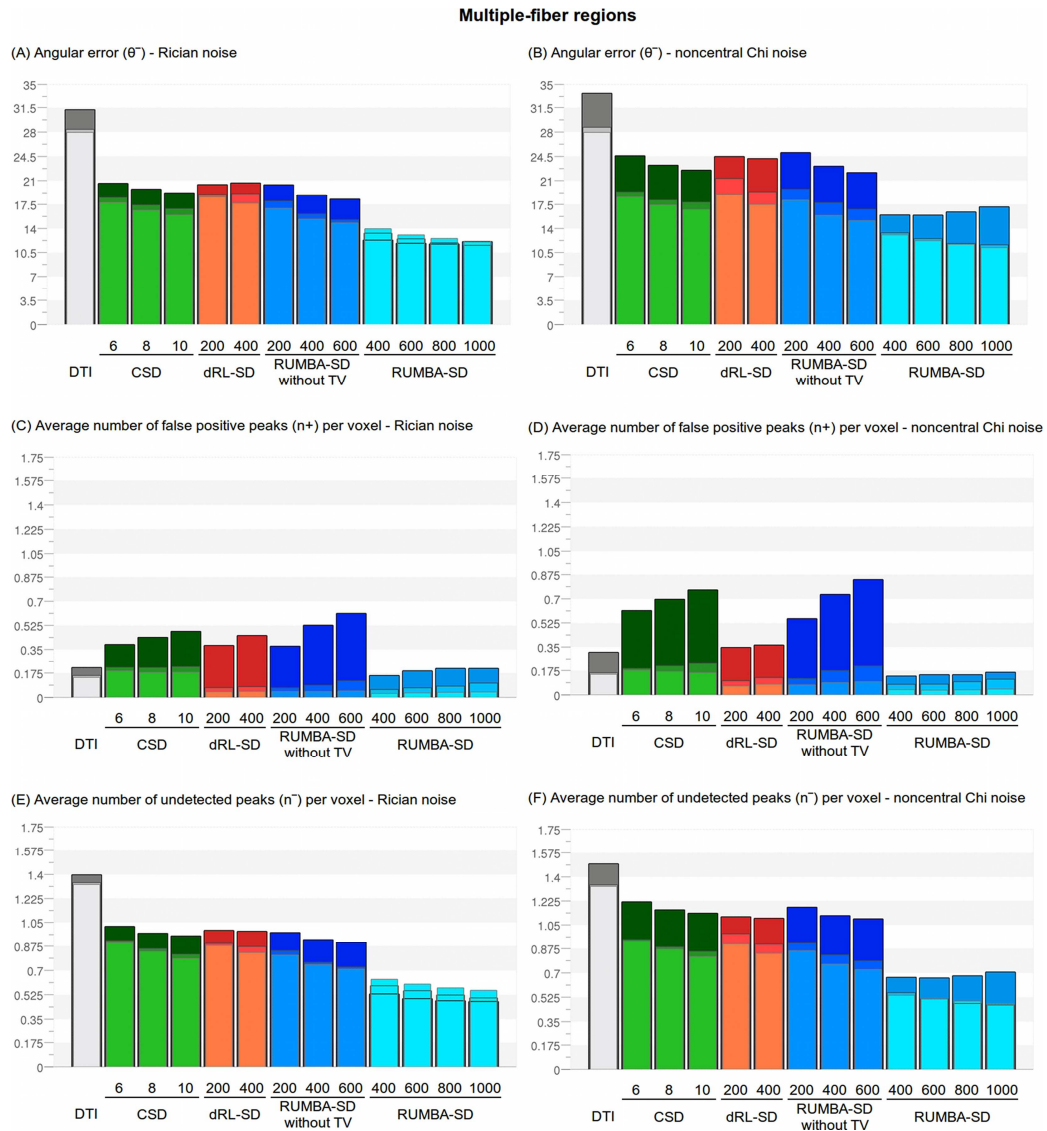


Figure 4. Quantification of the reconstruction accuracy of RUMBA-SD, RUMBA-SD without TV, dRL-SD, CSD and DTI in terms of $\bar{\theta}$ (angular error), n^+ (number of false positive) and n^- (number of false negative) in multiple-fiber regions of the phantom. Light colors indicate higher SNRs.

Figure 5 and Figure 6 depict normalized fiber ODF profiles estimated under different conditions. Normalization was performed by dividing the fiber ODF amplitudes by its maximum value in each voxel. In contrast to CSD, which does not allow estimating the volume fraction of the isotropic compartments, the fiber ODFs computed from dRL-SD and RUMBA-SD contain such volumes which, following (Dell'acqua et al., 2010), were added as constant terms along every direction. Specifically, Figure 5 shows the estimates from the SoS-based data generated with $SNR = 20$. Visual inspection shows that the RUMBA-SD higher performance could be related to the improved reconstruction accuracy in some complex regions. In particular, yellow arrows highlight voxels where RUMBA-SD was able to reconstruct fiber crossings with inter-fiber angles of 35-40 degrees, which were not detected by the other deconvolution techniques. The blue arrow highlights a region where RUMBA-SD was able to reconstruct fiber crossings with a low inter-fiber angle of 25 degrees. The red arrow highlights a region where RUMBA-SD was able to satisfactorily detect the non-dominant tract of a fiber crossing. It should be noted that fiber ODF profiles in isotropic regions were well represented by both dRL-SD and RUMBA-SD algorithms, whilst CSD produced a very noisy pattern in those regions. Moreover, the sharper fiber ODF profiles depicted by RUMBA-SD without TV, as compared to dRL-SD, could explain its superior ability to resolve fiber crossings.

Insert Figure 5 around here (1.5-2 columns)

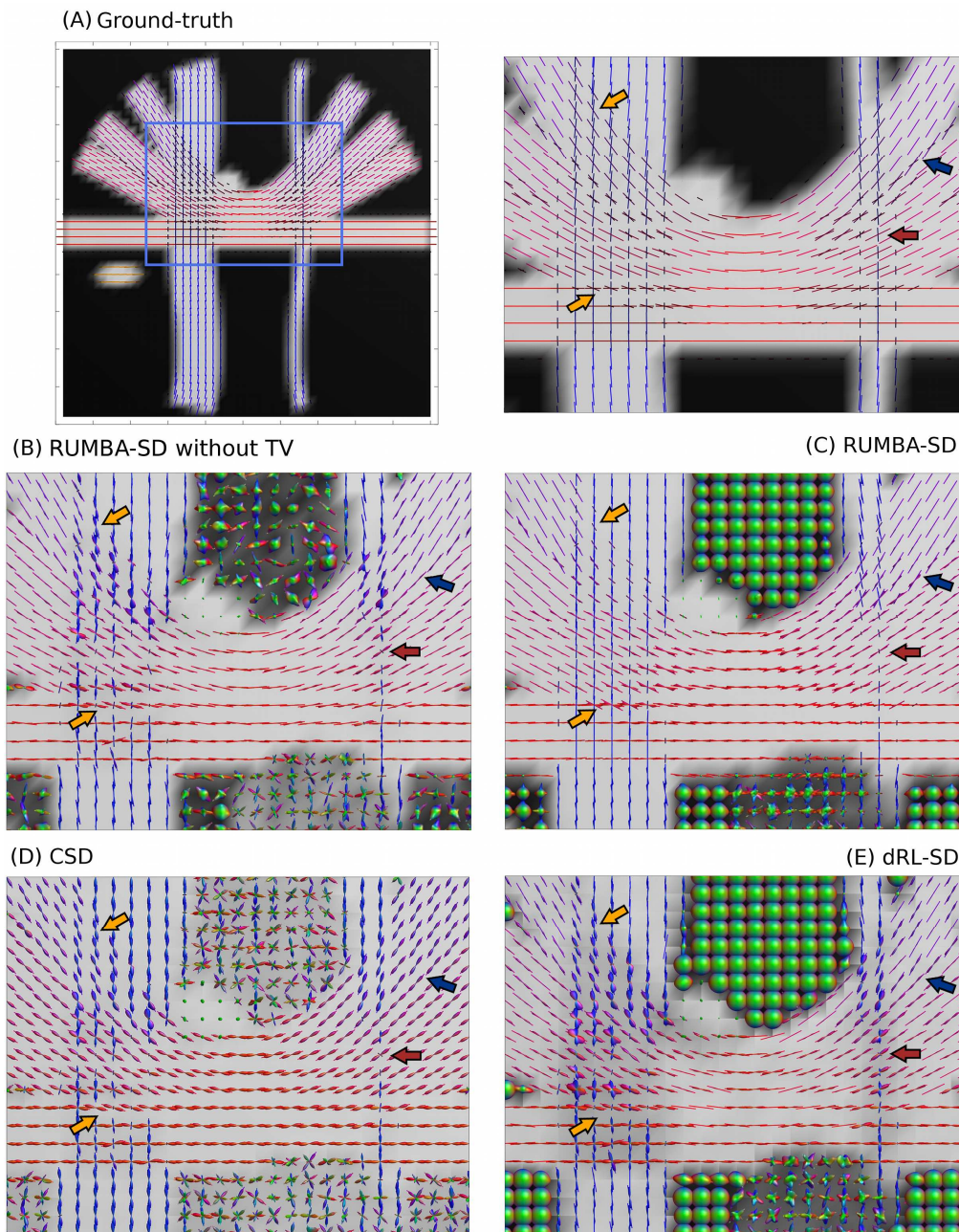


Figure 5. Visualization of the normalized fiber ODFs reconstructed from the SoS-based data generated with $\text{SNR} = 20$ in a coronal slice of the phantom. Depicted fiber ODF profiles correspond to the estimates from RUMBA-SD (using 1000 iterations), RUMBA-SD without TV (400 iterations) dRL-SD (400 iterations) and CSD (using $L_{\max} = 8$). Yellow arrows highlight voxels where RUMBA-SD was able to reconstruct fiber crossings with inter-fiber angles of 35-

40 degrees; blue arrow highlights a region where RUMBA-SD was able to reconstruct fiber crossings with inter-fiber angles of 25 degrees. The red arrow highlights a region where RUMBA-SD without TV, dRL-SD and CSD were not able to detect the non-dominant tract of a fiber crossing.

On the other hand, Figure 6 depicts the normalized fiber ODF estimates from the SMF-based data generated with $\text{SNR} = 10$ at the same slice used in Figure 5. RUMBA-SD without TV showed sharper fiber ODF profiles than those obtained from dRL-SD and CSD. At this low SNR, the benefit of using the TV regularization in RUMBA-SD again is visually corroborated.

Insert Figure 6 around here (1.5-2 columns)

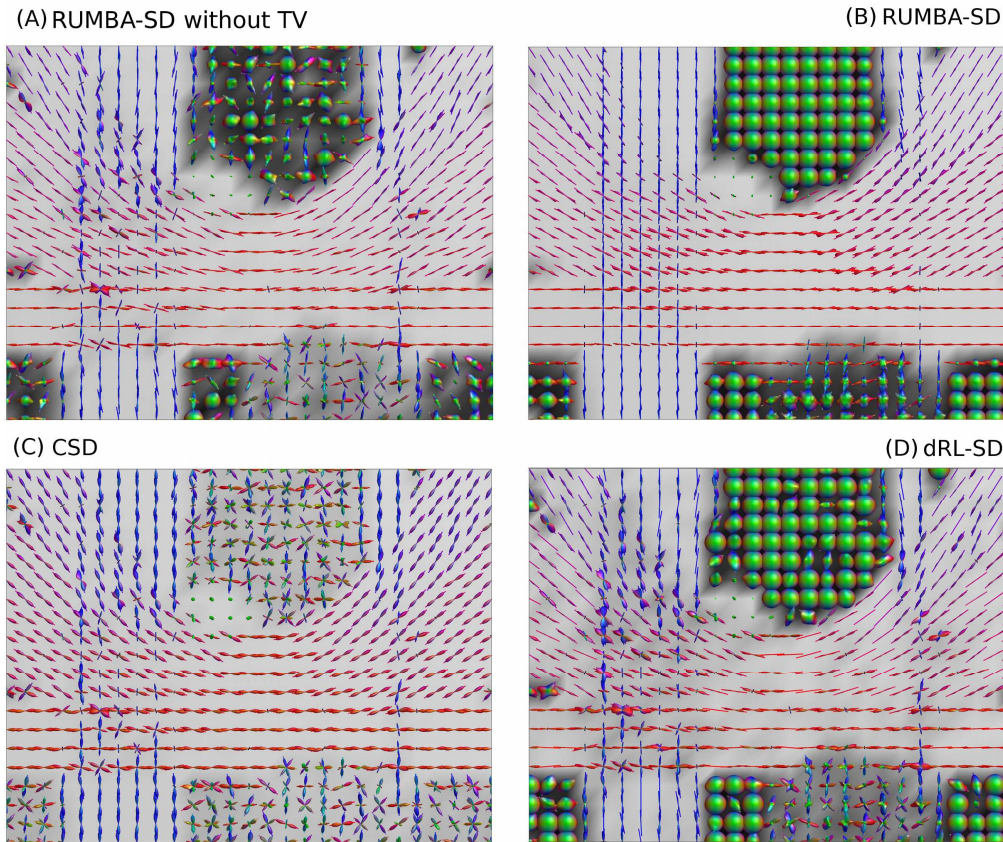


Figure 6. Visualization of the normalized fiber ODFs reconstructed from the SMF-based data generated with $\text{SNR} = 10$ in the same coronal slice of the phantom employed in Figure 5. Depicted fiber ODF profiles correspond to the estimates from RUMBA-SD (using 400 iterations), RUMBA-SD without TV (400 iterations) dRL-SD (400 iterations) and CSD (using $L_{\max} = 8$)

4.2 Real brain data

Fiber ODFs were estimated separately for each different SMF- and SoS-based dataset, including the original measured data with the full set of 256 gradient directions and their reduced forms comprised by subsets of 64 and 35 directions, respectively. In all cases, both RUMBA-SD and dRL-SD methods were implemented using the same dictionary, which was created assuming

diffusivities equal to $\lambda_1 = 1.0 \cdot 10^{-3} \text{ mm}^2/\text{s}$ and $\lambda_2 = \lambda_3 = 0.2 \cdot 10^{-3} \text{ mm}^2/\text{s}$, plus two isotropic terms with diffusivities equal to $0.6 \cdot 10^{-3} \text{ mm}^2/\text{s}$ and $1.4 \cdot 10^{-3} \text{ mm}^2/\text{s}$ (see Eqs.(1)-(3)). These values were selected to match the diffusivities obtained from a previous DTI fit in WM regions of parallel fibers, GM and CSF respectively. In CSD, the response function was measured from the images themselves in WM regions of parallel fibers (Tournier et al., 2008).

Figure 7 shows a coronal brain view with the normalized fiber ODFs and their maxima estimated from the full SMF-based data (i.e., data containing the full set of 256 gradient directions and 36 $b=0$ volumes). The computation time for each method is also reported in Table 2. Visual inspection of Fig. 7 reveals that all methods have produced quite similar reconstructions. Thus, while no spurious fibers in regions comprised by parallel fibers, like the midbody of the corpus callosum, was observed in any of the reconstructions, all approximations were able to resolve complex fiber geometries, like the mixture of tracts in the coronal plane located bilaterally at the intersection of the anterior limb of internal capsule, the external capsule and part of the superior longitudinal fasciculus. Between two and three fibers per voxel were detected by the different methods in this intersection, with RUMBA-SD being the method detecting three fibers in a major number of cases. However, such conclusions derived from visual inspection are limited by the fact that the underlying true anatomy is not known at the voxel level.

Insert Figure 7 around here (2 columns)

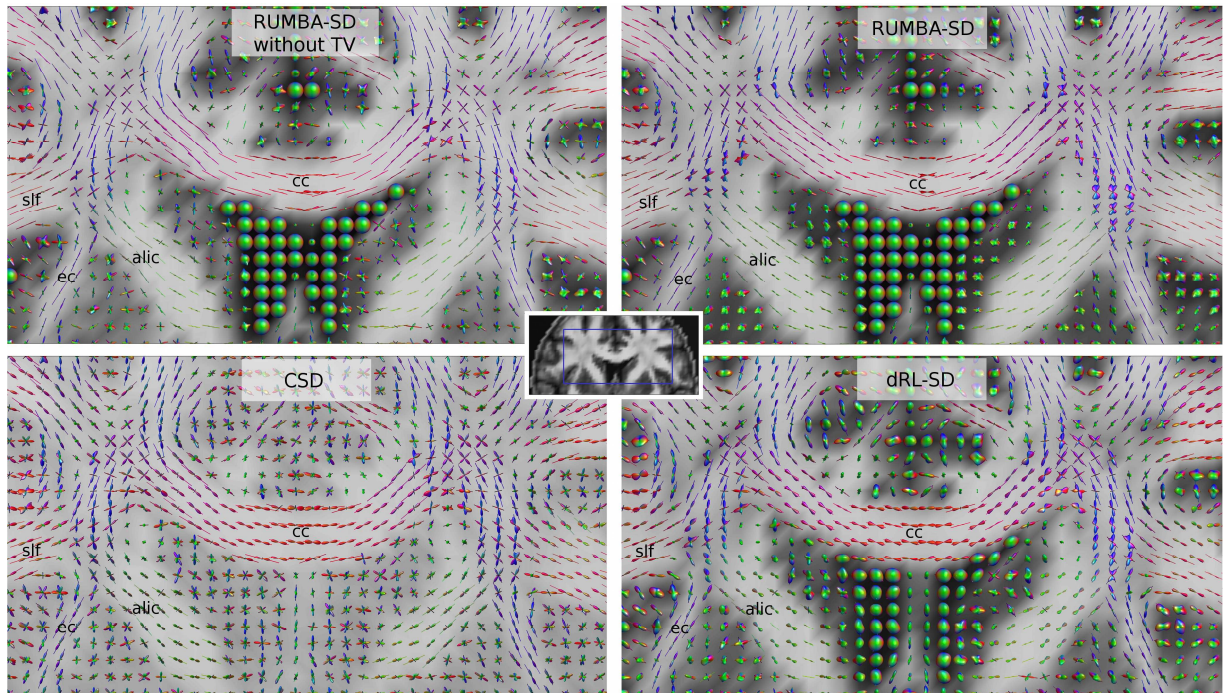


Figure 7. Visualization of the normalized fiber ODFs estimated in a coronal brain slice of the real multichannel diffusion MRI data combined via the SMF approach. Depicted fiber ODF profiles correspond to the estimates from RUMBA-SD (using 600 iterations), RUMBA-SD without TV (400 iterations) dRL-SD (400 iterations) and CSD (using $L_{\max} = 8$). The background images are the generalized fractional anisotropy images computed from each reconstruction. The following tracts are highlighted: alic (anterior limb of internal capsule), ec (external capsule), part of the slf (superior longitudinal fasciculus) and cc (corpus callosum). For simplicity only the tracts from the left part of the brain were labelled.

Insert Table 2 around here

Table 2. Time to fit the full real dataset required by each method tested in this study^(*)

Method	Computation time ^(**)
RUMBA-SD (using 600 iterations)	75 min
RUMBA-SD without TV (using 400 iterations)	14 min
dRL-SD (using 400 iterations)	10 min
CSD (using $L_{\max} = 8$).	12 min

^(*) Data containing the full set of 292 volumes (256 gradient directions plus 36 $b=0$ volumes); voxel size= $2 \times 2 \times 2$ mm³; volume size= $96 \times 96 \times 30$. All experiments have been conducted on a workstation with the following parameters: Intel Xeon(R) CPU X5680, 3.33 GHz x 12, 23.5 GB ram.

^(**) Computation time is only reported for the whole-brain spherical deconvolution estimation. Other processing steps like the peaks extraction from the estimated fiber ODFs were not considered. In the case of RUMBA-SD and dRL-SD methods the computation was performed using automatic multithreading in *Matlab*, whilst in CSD the computation was done by enabling the multithreading option in *MRtrix* software in 4 CPU cores.

In a further analysis we examined the ability of each method in reproducing original results (based on all gradient directions) using a reduced number of directions. Here, the angular correlations between fiber ODF estimates from the reduced datasets (i.e., 64 and 35 gradient directions) and the full SMF- and SoS-based data were calculated. Figure 8 shows the average correlations computed from all voxels within a brain mask created by thresholding the fractional anisotropy (FA) map, derived from DTI, at 0.2. As shown, RUMBA-SD provided the highest correlations between both SMF- and SoS-based data and the reduced datasets. Results from dRL-SD and RUMBA-SD without TV at low angular resolution were more reproducible than those

from CSD. In all cases, results based on 64 directions outperformed those based on 35 gradient directions.

Insert Figure 8 around here (1-1.5 columns)

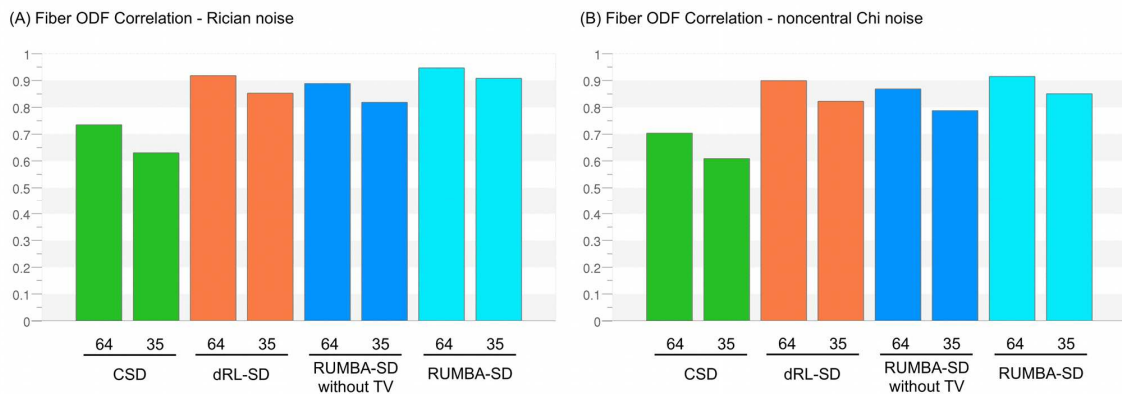


Figure 8. Mean correlation values between the fiber ODFs computed from the full set of measurements (i.e., 256 gradient directions + 36 $b=0$ images), which were considered as the gold standards, and from reduced datasets with lower number of measurements (i.e., 64 and 35 gradient directions + 3 $b=0$ images). Correlations were calculated in all voxels within a brain mask. Panel (A) shows results from the SMF-based datasets (corrupted with Rician noise), and panel (B) contains results from SoS-based datasets (corrupted by noncentral Chi noise).

In a final analysis we evaluated the capacity of each method in delivering similar results under the two different multichannel image combination approaches (i.e., SMF and SoS) considering, as well, a variable number of gradient directions. Figure 9 shows the average correlations computed from all voxels within the brain mask. Again, RUMBA-SD was the method providing the highest correlations between estimates from SMF- and SoS-based datasets. Notably, correlations computed in RUMBA-SD using 35 gradient directions were higher than those based on 64 directions using RUMBA-SD without TV, dRL-SD or CSD, suggesting a beneficial impact of TV regularization when data is acquired with a low number of gradient directions.

Insert Figure 9 around here (1 column)

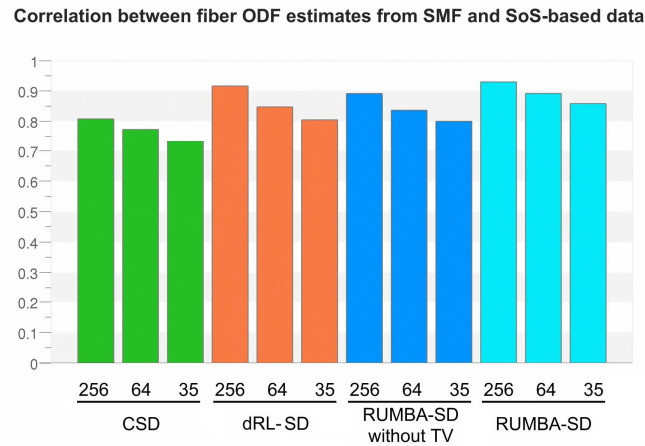


Figure 9. Mean correlation values between the fiber ODFs computed from different multichannel image combination approaches (i.e., SMF and SoS). The correlation was separately calculated for each pair of SMF- and SoS-based homologue datasets with equal number of measurements (i.e., number of gradient directions). The analysis was restricted to voxels within a brain mask.

5. DISCUSSION AND CONCLUSIONS

In this study we propose a new model-based spherical deconvolution method, RUMBA-SD. In contrast to previous diffusion reconstruction methods, usually based on Gaussian noise with zero mean, we consider Rician and noncentral Chi noise models, more adequate for characterizing the non-linear bias introduced in the images measured in current 1.5T and 3T multichannel MRI scanners. Although recent progress has been made in new SD methods adapted to corrupted Rician data, e.g., see (Clarke et al., 2008; Kaden and Kruggel, 2012) to the best of our knowledge, our study provides the first SD extension to noncentral Chi noise. Furthermore, RUMBA-SD offers a very general estimation framework applicable to different datasets. Its flexibility emanates from the explicit dependence between the likelihood model used and the real or effective number of coils in the scanner, and the methodology employed to combine multichannel signals. Moreover, the voxel-wise estimation of the noise variance allows a better adaptability to deviations in the shape of the noise distribution influenced, for instance, by use of accelerated MRI techniques and preprocessing steps. We hope that the proposed technique will help extending SD methods for a wide range of datasets taken from different scanners and using different protocols.

This study adds to previous diffusion MRI studies trying to overcome the signal-dependent bias introduced by the Rician and noncentral Chi noise. Among these studies, it has to be emphasized the recent noise filtering techniques described in (Brion et al., 2013; Koay et al., 2009), which may be applied in the pre-processing steps prior HARDI data estimation, as well as the robust DTI estimation methods in (Tristan-Vega et al., 2012) and the earlier DTI study conducted by (Salvador et al., 2005).

The relative performance of RUMBA-SD against two popular and powerful reconstruction algorithms, i.e., CSD and dRL-SD, has been evaluated using one of the finest diffusion MRI phantoms created to date. This phantom was particularly designed for the “HARDI Reconstruction Challenge 2013” Workshop, organized within the IEEE International Symposium on Biomedical Imaging. A previous version of RUMBA-SD took part in that challenge,

obtaining the first place in the ‘HARDI-like’ category (for more details see the website³; team name: ‘Capablanca’). The first-place was shared with a reconstruction based on the CSD method included in *Dipy* software⁴ (Garyfallidis et al., 2014). A manuscript on the ‘Challenge’ (currently under preparation) provides additional information about the performance of RUMBA-SD in relation to many other reconstruction methods not included in this work. In that sense, results here, fully based on local intra-voxel metrics, may be complemented with results in that paper, focused on global connectivity metrics derived from fiber tracking analyses.

In our work we have weighted the impact of Rician and noncentral Chi likelihood models through comparisons of outcomes from dRL-SD and ‘RUMBA-SD without TV’. Such comparisons, in contrast to those against CSD, were not biased by the use of different dictionaries and estimation algorithms. Both dRL-SD and RUMBA-SD without TV were implemented using the same dictionary of basis signals and similar reconstruction methods based on Richardson-Lucy algorithms adapted to Gaussian, Rician and noncentral Chi noise, respectively. Interestingly, dRL-SD had produced the lower number of spurious fiber orientations in single-fiber regions (see Fig. 3), demonstrating the benefit of the novel damping regularization procedure included in this algorithm (Dell’acqua et al., 2010). This performance is in line with a previous study comparing dRL-SD and CSD (Parker et al., 2013). On the other hand, RUMBA-SD without TV has showed a superior performance in multiple-fiber regions with sharper fiber ODF profiles (see Figs. 4 and 5), demonstrating the benefit of using proper likelihood models to speed the convergence of the algorithm and to increase our ability to resolve fiber crossings, a result that is consistent with a previous work developing a noise correction scheme for SD on Rician distributed data (Clarke et al., 2008).

CSD generated the highest number of spurious fibers in single-fiber regions, and had a performance similar to RUMBA-SD without TV in multiple-fiber regions. These results may be explained by the spherical harmonic basis used in CSD, effective at filtering noise and reducing the problem dimensionality but at the expense of secondary side-lobes arising from truncation of

³ http://hardi.epfl.ch/static/events/2013_ISBI/workshop.html#results

⁴ <http://nipy.org/dipy/>

the harmonic series. Here, though, it should be acknowledged that CSD and RUMBA-SD without TV used different approaches to create the signal dictionaries and, in consequence, results shown here cannot be taken as a proof of superiority for any of the two methods. The main purpose of including CSD in the evaluation was to obtain a practical estimation of the performance of the proposed method in relation to this state-of-the-art technique that is being extensively used in real applications.

Remarkably, when adequate likelihood models were combined with TV regularization (i.e. the full RUMBA-SD approach) the most accurate results were obtained for all metrics employed. TV regularization, apart from filtering noise has increased the ability to separate fiber bundles, as revealed both numerically (Figs. 3 and 4) and visually (Figs. 5 and 6).

When applied to human brain data, RUMBA-SD has also achieved the best results, and its reconstructions have shown the highest stability in front of differing noise types (characterized by SMF and SoS based datasets) and a reduced number of gradient directions (see Figs. 8 and 9). Interestingly, dRL-SD has also shown a performance superior to CSD, which may be explained by two aspects. While dRL-SD estimates had the smoothest fiber ODF profiles, contributing to obtain higher correlation values, results from CSD were probably affected by its worse performance in voxels with mixtures of WM, GM and CSF (Roine et al., 2014) contributing to the reduction in mean correlation values (see Fig. 7).

A recent study has demonstrated that the SoS approach produces a signal-dependent bias that reduces the signal dynamic range and may subsequently lead to reduced precision and accuracy in fiber orientation estimates (Sotiropoulos et al., 2013). Our study, however, suggests that the noncentral Chi noise in SoS-based data is not a major concern for the SD methods considered. For instance, heavier squashing of fiber ODFs when SoS reconstruction is used (Sotiropoulos et al., 2013) is not that prominent with SD approaches, compared to diffusion ODF estimation methods (Aganj et al., 2010). This result may have several possible explanations specific to each technique. Thus, the robustness of CSD may be explained by the fact that the dictionary of basis signals is directly created by averaging the measured signals and, in consequence, the noise bias is already included in the dictionary. Although this would not allow cancelling the bias in brain

regions composed of multiple fibers, because the bias is non-linear and signal-dependent, the final results are less sensitive to it. On the other hand, the robustness of dRL-SD may be explained, in part, by its lower over-all sensitivity to selection of the response function (Parker et al., 2013), which make it robust to the use of dictionaries estimated from either biased or unbiased signals; behaviour that may be additionally boosted by the inclusion of the damping factor in the RL algorithm. Finally, the robustness of RUMBA-SD can be explained by the use of proper likelihood models that explicitly consider the bias as function of the noise corrupting the data. However, it should be noted that the satisfactory performance of RUMBA-SD has been significantly improved by the introduction of a total variation spatial regularization on the fiber ODF field, adaptively incorporated into the estimation process.

At this point, it is important to highlight the differences between the ‘unified approach’ used in this work for joint estimation and filtering, and previous strategies based on denoising the raw diffusion MRI data prior to the actual SD reconstruction. The main advantage of the latter approaches is that they may benefit from including state-of-art advanced denoising algorithms. This was exemplified in the reconstruction ‘Challenge’ described above, where the other winning SD technique in the ‘HARDI-like’ category, namely CSD, incorporated a sophisticated adaptative non-local means denoising method (Manjon et al., 2010). Conversely, the main advantage of the unified approach proposed here is that it provides a precise model to distinguish real signals from noise throughout all the 4D diffusion MRI data. In contrast, many of the advanced denoising algorithms that are currently being applied in isolation were developed to filter volumetric (3D) data, and thus process each 3D image of the 4D series independently, without considering the implicit orientation dependence of the measurements. In that sense, and from a conceptual point of view, the unified approach described in this work provides a more general estimation framework, which could be extended in future to include similarity measures like those employed in advanced denoising algorithms (Manjon et al., 2010), thus allowing merging the main benefits of both strategies.

To finish, some limitations and possible future extensions of the study should be acknowledged. First, while our results were based on a single phantom, one would expect slightly different results if methods were run on other datasets, requiring new data to derive definitive conclusions

about the behavior of each methodology under diverse situations. Second, we have not evaluated the proposed method in synthetic data simulating partial Fourier k -space acquisitions and parallel imaging methods with various acceleration factors (i.e., $R>1$), yet it may be interesting to consider it in the future. Third, the estimation framework in RUMBA-SD is based on a discrete approximation of the fiber ODF, and it may be potentially extended to continuous functions on the sphere, like spherical harmonics and wavelets. Fourth, the TV regularization implemented in this study is based on a channel-by-channel first order scheme. New studies may compare different regularization techniques such as higher order TV, vectorial TV and the fiber continuity function introduced in (Reisert and Kiselev, 2011), to mention only a few examples. Fifth, different strategies for creating the signal dictionary could be explored, like using mixtures of intra-compartment models to capture different diffusion profiles, or applying more appropriate models to fit multi-shell data (Jbabdi et al., 2012; Jeurissen et al., 2014). Similarly, the recursive calibration of the single-fiber response function (Tax et al., 2014) may be another possible implementation. On the other hand, the linear inversion framework used in RUMBA-SD is not limited to fiber ODF reconstructions, but it could be applied also to improve microstructure imaging methods such as ActiveAx and NODDI. In fact, it was recently showed in that this class of techniques can be reformulated as convenient linear systems (Daducci et al., 2014b). The formulation in (Daducci et al., 2014b) is based, as most of the existing deconvolution approaches, on the Gaussian assumption about the noise; likewise, the estimation is performed on a voxel-by-voxel basis. Notably, the RUMBA-SD iterative scheme proposed in this work addresses both limitations and could potentially lead to improved reconstructions also in the case of microstructure imaging. Finally, a critical point of SD methods is their assumption of a common response function for all brain tracts, and future studies should be oriented towards the minimization of the impact of this approximation. In that direction, we envisage two different estimation frameworks which may be adapted to the SD context. One of them is penalized total least squares (TLS), which provides a more natural way to model the data when both measured signal and assumed dictionary are contaminated by ‘errors’. Here, a TLS-based SD method may be effective in reducing the sensitivity to the selection of the response function by adding information about the range of variability expected for it. The other one is nonparametric blind

deconvolution, which offers the possibility of estimating different response functions at each voxel without assuming predefined generative models.

6. ACKNOWLEDGMENTS

This work was supported by the Catalanian Government (2009SGR211 to the Research Unit of FIDMAG) and several grants from the Plan Nacional de I+D+i and co-funded by the Instituto de Salud Carlos III-Subdirección General de Evaluación y Fomento de la Investigación and the European Regional Development Fund (FEDER): Miguel Servet Research Contracts (CP07/00048 to RS and CP10/00596 to EP-C) and Rio Hortega Research Contract (CM11/00024 to JR). The funding organizations played no role in the study design, data collection and analysis, or manuscript approval. Also, we would like to thank Dr Karla Miller for assisting us with data collection. The presented study is a tribute to composers who popularized Rumba music in the 1940s and 50s, including Dámaso Pérez Prado, Mongo Santamaría, Xavier Cugat, and Chano Pozo.

APPENDICES

A – Relationship with the RL-SD method

In the limit of very high signal to noise ratio (i.e., $\mathbf{S} \circ \mathbf{H}\mathbf{f}^k / \sigma^2 \gg n$) the modified Bessel functions ratio in Eq. (8) tends to the unity (see Figure 10). In that limit, Eq. (8) becomes:

$$\mathbf{f}^{k+1} = \mathbf{f}^k \circ \frac{\mathbf{H}^T \mathbf{S}}{\mathbf{H}^T \mathbf{H} \mathbf{f}^k}, \quad (\text{A-1})$$

which is just the undamped RL-SD method originally proposed in (Dell'Acqua et al., 2007) under the assumption of zero-mean Gaussian noise .

B – Noncentral Chi noise model for SoS data - effective or standard values?

As previously discussed, for scanners with a high number of coils where the effect of noise correlation cannot be easily decoupled, a best approximation for the noise model in SoS-based images is obtained by using effective n_{eff} and σ_{eff}^2 values (Aja-Fernandez and Tristan-Vega, 2012). This section is devoted to provide an initial insight on the implication of using a noncentral Chi noise model in our estimation with standard parameters, instead of the effective ones.

If considering the limit $n \gg 1$, the ratio provided by Eq. (C-1) in Appendix C can be approximated as:

$$\frac{I_n(x)}{I_{n-1}(x)} \approx \frac{x}{n + \sqrt{x^2 + n^2}}, \quad (\text{B-1})$$

where we have used the identity relating the expansion of a square root in terms of continued fraction. This expression can be regarded as a lower bound for the true ratio, which is more accurate insofar as n increases.

Notably, based on this result we obtain

$$\frac{I_n(\mathbf{S} \circ \mathbf{Hf} / \sigma^2)}{I_{n-1}(\mathbf{S} \circ \mathbf{Hf} / \sigma^2)} \approx \frac{\mathbf{S} \circ \mathbf{Hf}}{n\sigma^2 + \sqrt{(\mathbf{S} \circ \mathbf{Hf})^2 + (n\sigma^2)^2}}. \quad (\text{B-2})$$

Similarly,

$$\frac{I_{n_{eff}}(\mathbf{S} \circ \mathbf{Hf} / \sigma_{eff}^2)}{I_{n_{eff}-1}(\mathbf{S} \circ \mathbf{Hf} / \sigma_{eff}^2)} \approx \frac{\mathbf{S} \circ \mathbf{Hf}}{n_{eff}\sigma_{eff}^2 + \sqrt{(\mathbf{S} \circ \mathbf{Hf})^2 + (n_{eff}\sigma_{eff}^2)^2}}. \quad (\text{B-3})$$

The relevant feature of these relationships is that they do not depend on the individual parameters of interest but just on their products $n\sigma^2$ and $n_{eff}\sigma_{eff}^2$. This implies that although in general the functions $I_n(\mathbf{S} \circ \mathbf{Hf} / \sigma^2)$ and $I_{n_{eff}}(\mathbf{S} \circ \mathbf{Hf} / \sigma_{eff}^2)$ are different, if $n_{eff}\sigma_{eff}^2 = n\sigma^2$ then their ratios (which are the terms used in the computation) satisfy:

$$\frac{I_n(\mathbf{S} \circ \mathbf{Hf} / \sigma^2)}{I_{n-1}(\mathbf{S} \circ \mathbf{Hf} / \sigma^2)} \approx \frac{I_{n_{eff}}(\mathbf{S} \circ \mathbf{Hf} / \sigma_{eff}^2)}{I_{n_{eff}-1}(\mathbf{S} \circ \mathbf{Hf} / \sigma_{eff}^2)}. \quad (\text{B-4})$$

The accuracy of this approximation is determined by the accuracy of Eq. (B-1) and the assumption $n_{eff}\sigma_{eff}^2 = n\sigma^2$. Interestingly, in (Dietrich et al., 2008) was reported that for a system with 32 receiver channels of non-accelerated SoS-based data, the mean effective number of channels was $n_{eff}=12$. Theoretical calculations in (Aja-Fernandez and Tristan-Vega, 2012)

predict similar n_{eff} values for 32 and 16 coil systems with correlation coefficients between coil of $\rho \approx 0.3$ and $\rho \approx 0.2$, respectively. In a complementary analysis (result not shown) we have verified that Eq. (B-1) provides a ‘reasonable’ approximation for that effective number of channels. Moreover, in (Aja-Fernandez et al., 2013) was showed that for SoS reconstructions without using fast pMRI techniques the product $n_{eff}\sigma_{eff}^2$ is constant across the image and equal to $n\sigma^2$. These results, taken together, indicate that for *non-accelerated* SoS-based data acquired in multichannel scanners with a high number of coils and moderate correlation coefficients between coils the SD estimation process may be approximately performed using the standard parameters. That is, by working in terms of the real parameters n and σ^2 , we can avoid the complex estimation of the spatial-dependent effective parameters.

C – A note on the evaluation of the term $I_n(x)/I_{n-1}(x)$

The proposed SD algorithm involves the evaluation of the ratio of modified Bessel functions of first kind. Such evaluation is best computed by considering the ratio as a new composite function, and not by means of the simple evaluation of the ratio of the individual functions. The main reason for this is related to the divergence towards infinity of the individual functions. For instance, in *Matlab* software, numerical values for $I_n(x)$ are only available for $x \leq 700$; for higher values an infinity value is returned, and thus the ratio cannot be computed.

Interestingly, this ratio can be expressed in terms of Perron continued fraction (Gautschi and Slavik, 1978):

$$\frac{I_n(x)}{I_{n-1}(x)} = \frac{x}{2n+x - \frac{2x(n+1/2)}{2n+1+2x - \frac{2x(n+3/2)}{2n+2+2x - \frac{2x(n+5/2)}{2n+3+2x - \ddots}}}} \quad (\text{C-1})$$

A study about the convergence of this expansion (Gautschi and Slavik, 1978) revealed that it converges faster than other analogous representation based on Gauss continued fraction. For the purpose of this application, the summation in Eq. (C-1) is performed up to the final term $\frac{2x(n+5/2)}{2n+3+2x}$. Figure 10 shows the accuracy of this approximation for different values of n and for a wide range of values of x .

Insert Figure 10 around here (1 column)

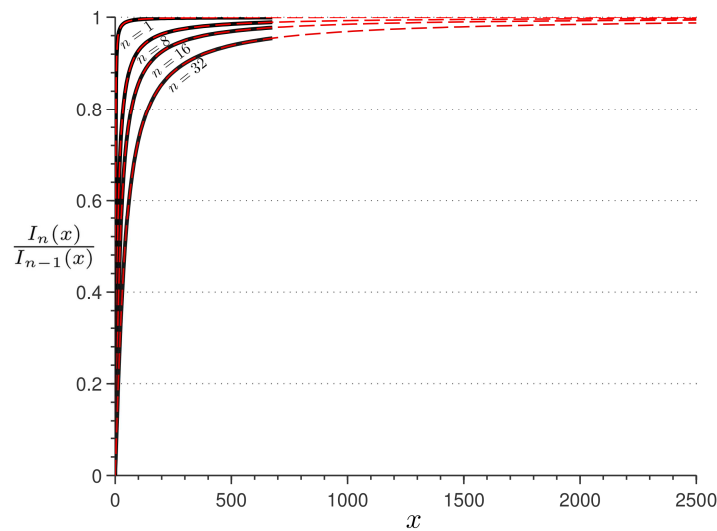


Figure 10. Ratio of modified Bessel functions of first kind. Black continuous curves denote the exact values computed by means of the evaluation of the ratio of the individual Bessel functions. The fast divergence towards infinity of the individual functions does not allow evaluating this expression for the whole range of values. Red discontinuous curves denote the values computed by means of the Perron continued fraction approximation in Eq. (C-1) in the whole range of values.

REFERENCES

- Aganj, I., Lenglet, C., Sapiro, G., Yacoub, E., Ugurbil, K., Harel, N., 2010. Reconstruction of the orientation distribution function in single- and multiple-shell q-ball imaging within constant solid angle. *Magn Reson Med* 64, 554-566.
- Aja-Fernandez, S., Brion, V., Tristan-Vega, A., 2013. Effective noise estimation and filtering from correlated multiple-coil MR data. *Magn Reson Imaging* 31, 272-285.
- Aja-Fernandez, S., Tristan-Vega, A., 2012. Influence of noise correlation in multiple-coil statistical models with sum of squares reconstruction. *Magn Reson Med* 67, 580-585.
- Aja-Fernandez, S., Tristan-Vega, A., Alberola-Lopez, C., 2009. Noise estimation in single- and multiple-coil magnetic resonance data based on statistical models. *Magn Reson Imaging* 27, 1397-1409.
- Aja-Fernandez, S., Tristan-Vega, A., Hoge, W.S., 2011. Statistical noise analysis in GRAPPA using a parametrized noncentral Chi approximation model. *Magn Reson Med* 65, 1195-1206.
- Aja-Fernandez, S., Vegas-Sanchez-Ferrero, G., Tristan-Vega, A., 2014. Noise estimation in parallel MRI: GRAPPA and SENSE. *Magn Reson Imaging* 32, 281-290.
- Alexander, D.C., 2005. Maximum entropy spherical deconvolution for diffusion MRI. *Inf Process Med Imaging* 19, 76-87.
- Anderson, A.W., 2005. Measurement of fiber orientation distributions using high angular resolution diffusion imaging. *Magn Reson Med* 54, 1194-1206.
- Assemlal, H.E., Tschumperle, D., Brun, L., Siddiqi, K., 2011. Recent advances in diffusion MRI modeling: Angular and radial reconstruction. *Med Image Anal* 15, 369-396.
- Basser, P.J., Mattiello, J., LeBihan, D., 1994. Estimation of the effective self-diffusion tensor from the NMR spin echo. *J Magn Reson B* 103, 247-254.
- Behrens, T.E., Berg, H.J., Jbabdi, S., Rushworth, M.F., Woolrich, M.W., 2007. Probabilistic diffusion tractography with multiple fibre orientations: What can we gain? *Neuroimage* 34, 144-155.
- Behrens, T.E., Woolrich, M.W., Jenkinson, M., Johansen-Berg, H., Nunes, R.G., Clare, S., Matthews, P.M., Brady, J.M., Smith, S.M., 2003. Characterization and propagation of uncertainty in diffusion-weighted MR imaging. *Magn Reson Med* 50, 1077-1088.

Blaimer, M., Breuer, F., Mueller, M., Heidemann, R.M., Griswold, M.A., Jakob, P.M., 2004. SMASH, SENSE, PILS, GRAPPA: how to choose the optimal method. *Top Magn Reson Imaging* 15, 223-236.

Brion, V., Poupon, C., Riff, O., Aja-Fernandez, S., Tristan-Vega, A., Mangin, J.F., Le Bihan, D., Poupon, F., 2013. Noise correction for HARDI and HYDI data obtained with multi-channel coils and Sum of Squares reconstruction: An anisotropic extension of the LMMSE. *Magn Reson Imaging* 31, 1360-1371.

Canales-Rodríguez, E.J., Iturria-Medina, Y., Aleman-Gomez, Y., Melie-Garcia, L., 2010a. Deconvolution in diffusion spectrum imaging. *Neuroimage* 50, 136-149.

Canales-Rodríguez, E.J., Lin, C.P., Iturria-Medina, Y., Yeh, C.H., Cho, K.H., Melie-Garcia, L., 2010b. Diffusion orientation transform revisited. *Neuroimage* 49, 1326-1339.

Canales-Rodríguez, E.J., Melie-Garcia, L., Iturria-Medina, Y., 2009. Mathematical description of q-space in spherical coordinates: exact q-ball imaging. *Magn Reson Med* 61, 1350-1367.

Canales-Rodríguez, E.J., Melie-Garcia, L., Iturria-Medina, Y., Martinez-Montes, E., Aleman-Gomez, Y., Lin, C.P., 2008. Inferring multiple maxima in intravoxel white matter fiber distribution. *Magn Reson Med* 60, 616-630.

Chambolle, A., 2004. An algorithm for total variation minimization and applications. *Journal of Mathematical Imaging and Vision* 20, 89-97.

Clarke, R.A., Scifo, P., Rizzo, G., Dell'Acqua, F., Scotti, G., Fazio, F., 2008. Noise correction on Rician distributed data for fibre orientation estimators. *IEEE Trans Med Imaging* 27, 1242-1251.

Constantinides, C.D., Atalar, E., McVeigh, E.R., 1997. Signal-to-noise measurements in magnitude images from NMR phased arrays. *Magn Reson Med* 38, 852-857.

Daducci, A., Canales-Rodríguez, E.J., Descoteaux, M., Garyfallidis, E., Gur, Y., Ying-Chia, L., Mani, M., Merlet, S., Paquette, M., Ramirez-Manzanares, A., Reisert, M., Reis Rodrigues, P., Seppeband, F., Caruyer, E., Choupan, J., Deriche, R., Jacob, M., Menegaz, G., Prckovska, V., Rivera, M., Wiaux, Y., Thiran, J.P., 2014a. Quantitative Comparison of Reconstruction Methods for Intra-Voxel Fiber Recovery From Diffusion MRI. *Medical Imaging, IEEE Transactions on* 33, 384-399.

Daducci, A., Canales-Rodríguez, E.J., Zhang, H., Dyrby, T.B., Alexander, D.C., Thiran, J.-P., 2014b. Accelerated Microstructure Imaging via Convex Optimization (AMICO) from diffusion MRI data. *Neuroimage* (In press).

Daducci, A., Van De Ville, D., Thiran, J.P., Wiaux, Y., 2014c. Sparse regularization for fiber ODF reconstruction: from the suboptimality of l2 and l1 priors to l0. *Med Image Anal* 18, 820-833.

Dell'Acqua, F., Rizzo, G., Scifo, P., Clarke, R.A., Scotti, G., Fazio, F., 2007. A model-based deconvolution approach to solve fiber crossing in diffusion-weighted MR imaging. *IEEE Trans Biomed Eng* 54, 462-472.

Dell'acqua, F., Scifo, P., Rizzo, G., Catani, M., Simmons, A., Scotti, G., Fazio, F., 2010. A modified damped Richardson-Lucy algorithm to reduce isotropic background effects in spherical deconvolution. *Neuroimage* 49, 1446-1458.

Descoteaux, M., Angelino, E., Fitzgibbons, S., Deriche, R., 2007. Regularized, fast, and robust analytical Q-ball imaging. *Magn Reson Med* 58, 497-510.

Descoteaux, M., Deriche, R., Knosche, T.R., Anwander, A., 2009. Deterministic and probabilistic tractography based on complex fibre orientation distributions. *IEEE Trans Med Imaging* 28, 269-286.

Descoteaux, M., Deriche, R., Le Bihan, D., Mangin, J.F., Poupon, C., 2011. Multiple q-shell diffusion propagator imaging. *Med Image Anal* 15, 603-621.

Dey, N., Blanc-Feraud, L., Zimmer, C., Roux, P., Kam, Z., Olivo-Marin, J.C., Zerubia, J., 2006. Richardson-Lucy algorithm with total variation regularization for 3D confocal microscope deconvolution. *Microsc Res Tech* 69, 260-266.

Dietrich, O., Raya, J.G., Reeder, S.B., Ingrisch, M., Reiser, M.F., Schoenberg, S.O., 2008. Influence of multichannel combination, parallel imaging and other reconstruction techniques on MRI noise characteristics. *Magn Reson Imaging* 26, 754-762.

Fillard, P., Descoteaux, M., Goh, A., Gouttard, S., Jeurissen, B., Malcolm, J., Ramirez-Manzanares, A., Reisert, M., Sakaie, K., Tensaouti, F., Yo, T., Mangin, J.F., Poupon, C., 2011. Quantitative evaluation of 10 tractography algorithms on a realistic diffusion MR phantom. *Neuroimage* 56, 220-234.

Garyfallidis, E., Brett, M., Amirbekian, B., Rokem, A., Van Der Walt, S., Descoteaux, M., Nimmo-Smith, I., 2014. Dipy, a library for the analysis of diffusion MRI data. *Front. Neuroinform.* 8:8.

Gautschi, W., Slavik, J., 1978. On the Computation of Modified Bessel Function Ratios. *MATHEMATICS OF COMPUTATION* 32, 865-875.

Gudbjartsson, H., Patz, S., 1995. The Rician distribution of noisy MRI data. *Magn Reson Med* 34, 910-914.

Hagmann, P., Cammoun, L., Gigandet, X., Meuli, R., Honey, C.J., Wedeen, V.J., Sporns, O., 2008. Mapping the structural core of human cerebral cortex. *PLoS Biol* 6, e159.

Henkelman, R.M., 1985. Measurement of signal intensities in the presence of noise in MR images. *Med Phys* 12, 232-233.

Hess, C.P., Mukherjee, P., Han, E.T., Xu, D., Vigneron, D.B., 2006. Q-ball reconstruction of multimodal fiber orientations using the spherical harmonic basis. *Magn Reson Med* 56, 104-117.

Hosseini, A.P., Chung, M.K., Wu, Y.C., Alexander, A.L., 2013. Bessel Fourier Orientation Reconstruction (BFOR): an analytical diffusion propagator reconstruction for hybrid diffusion imaging and computation of q-space indices. *Neuroimage* 64, 650-670.

Iturria-Medina, Y., Perez Fernandez, A., Morris, D.M., Canales-Rodríguez, E.J., Haroon, H.A., Garcia Penton, L., Augath, M., Galan Garcia, L., Logothetis, N., Parker, G.J., Melie-Garcia, L., 2011. Brain hemispheric structural efficiency and interconnectivity rightward asymmetry in human and nonhuman primates. *Cereb Cortex* 21, 56-67.

Iturria-Medina, Y., Sotero, R.C., Canales-Rodríguez, E.J., Aleman-Gomez, Y., Melie-Garcia, L., 2008. Studying the human brain anatomical network via diffusion-weighted MRI and Graph Theory. *Neuroimage* 40, 1064-1076.

Jbabdi, S., Sotiropoulos, S.N., Savio, A.M., Grana, M., Behrens, T.E., 2012. Model-based analysis of multishell diffusion MR data for tractography: how to get over fitting problems. *Magn Reson Med* 68, 1846-1855.

Jensen, J.H., Helpert, J.A., Ramani, A., Lu, H., Kaczynski, K., 2005. Diffusional kurtosis imaging: the quantification of non-gaussian water diffusion by means of magnetic resonance imaging. *Magn Reson Med* 53, 1432-1440.

Jeurissen, B., Tournier, J.D., Dhollander, T., Connelly, A., Sijbers, J., 2014. Multi-tissue constrained spherical deconvolution for improved analysis of multi-shell diffusion MRI data. *Neuroimage*.

Jian, B., Vemuri, B.C., 2007. A unified computational framework for deconvolution to reconstruct multiple fibers from diffusion weighted MRI. *IEEE Trans Med Imaging* 26, 1464-1471.

Kaden, E., Knosche, T.R., Anwender, A., 2007. Parametric spherical deconvolution: inferring anatomical connectivity using diffusion MR imaging. *Neuroimage* 37, 474-488.

Kaden, E., Kruggel, F., 2012. Nonparametric Bayesian inference of the fiber orientation distribution from diffusion-weighted MR images. *Med Image Anal* 16, 876-888.

Keil, B., Wald, L.L., 2013. Massively parallel MRI detector arrays. J Magn Reson 229, 75-89.

Koay, C.G., Ozarslan, E., Basser, P.J., 2009. A signal transformational framework for breaking the noise floor and its applications in MRI. J Magn Reson 197, 108-119.

Landman, B.A., Bogovic, J.A., Wan, H., El Zahraa ElShahaby, F., Bazin, P.L., Prince, J.L., 2012. Resolution of crossing fibers with constrained compressed sensing using diffusion tensor MRI. Neuroimage 59, 2175-2186.

Liu, C., Bammer, R., Acar, B., Moseley, M.E., 2004. Characterizing non-Gaussian diffusion by using generalized diffusion tensors. Magn Reson Med 51, 924-937.

Lucy, L.B., 1974. An iterative technique for the rectification of observed distributions. Astron. J. 79, 745-754.

Manjon, J.V., Coupe, P., Marti-Bonmati, L., Collins, D.L., Robles, M., 2010. Adaptive non-local means denoising of MR images with spatially varying noise levels. J Magn Reson Imaging 31, 192-203.

Melie-Garcia, L., Canales-Rodríguez, E.J., Aleman-Gomez, Y., Lin, C.P., Iturria-Medina, Y., Valdes-Hernandez, P.A., 2008. A Bayesian framework to identify principal intravoxel diffusion profiles based on diffusion-weighted MR imaging. Neuroimage 42, 750-770.

Michailovich, O., Rathi, Y., Dolui, S., 2011. Spatially regularized compressed sensing for high angular resolution diffusion imaging. IEEE Trans Med Imaging 30, 1100-1115.

Ozarslan, E., Mareci, T.H., 2003. Generalized diffusion tensor imaging and analytical relationships between diffusion tensor imaging and high angular resolution diffusion imaging. Magn Reson Med 50, 955-965.

Ozarslan, E., Shepherd, T.M., Vemuri, B.C., Blackband, S.J., Mareci, T.H., 2006. Resolution of complex tissue microarchitecture using the diffusion orientation transform (DOT). Neuroimage 31, 1086-1103.

Parker, G.D., Marshall, D., Rosin, P.L., Drage, N., Richmond, S., Jones, D.K., 2013. A pitfall in the reconstruction of fibre ODFs using spherical deconvolution of diffusion MRI data. Neuroimage 65, 433-448.

Patel, V., Shi, Y., Thompson, P.M., Toga, A.W., 2010. Mesh-based spherical deconvolution: a flexible approach to reconstruction of non-negative fiber orientation distributions. Neuroimage 51, 1071-1081.

Pruessmann, K.P., Weiger, M., Scheidegger, M.B., Boesiger, P., 1999. SENSE: sensitivity encoding for fast MRI. *Magn Reson Med* 42, 952-962.

Ramirez-Manzanares, A., Rivera, M., Vemuri, B.C., Carney, P., Mareci, T., 2007. Diffusion basis functions decomposition for estimating white matter intravoxel fiber geometry. *IEEE Trans Med Imaging* 26, 1091-1102.

Reisert, M., Kiselev, V.G., 2011. Fiber continuity: an anisotropic prior for ODF estimation. *IEEE Trans Med Imaging* 30, 1274-1283.

Richardson, W.H., 1972. Bayesian-based iterative method of image restoration. *J Opt. Soc. Am.* 62, 55–59.

Roine, T., Jeurissen, B., Perrone, D., Aelterman, J., Leemans, A., Philips, W., Sijbers, J., 2014. Isotropic non-white matter partial volume effects in constrained spherical deconvolution. *Front Neuroinform* 8, 28.

Rudin, L.I., Osher, S., Fatemi, E., 1992. Nonlinear total variation based noise removal algorithms. *Physica D* 60, 259–268.

Salat, D.H., Tuch, D.S., Greve, D.N., van der Kouwe, A.J., Hevelone, N.D., Zaleta, A.K., Rosen, B.R., Fischl, B., Corkin, S., Rosas, H.D., Dale, A.M., 2005. Age-related alterations in white matter microstructure measured by diffusion tensor imaging. *Neurobiol Aging* 26, 1215-1227.

Salvador, R., Pena, A., Menon, D.K., Carpenter, T.A., Pickard, J.D., Bullmore, E.T., 2005. Formal characterization and extension of the linearized diffusion tensor model. *Hum Brain Mapp* 24, 144-155.

Smith, S.M., Jenkinson, M., Woolrich, M.W., Beckmann, C.F., Behrens, T.E., Johansen-Berg, H., Bannister, P.R., De Luca, M., Drobnjak, I., Flitney, D.E., Niazy, R.K., Saunders, J., Vickers, J., Zhang, Y., De Stefano, N., Brady, J.M., Matthews, P.M., 2004. Advances in functional and structural MR image analysis and implementation as FSL. *Neuroimage* 23 Suppl 1, S208-219.

Söderman, O., Jönsson, B., 1995. Restricted diffusion in cylindrical geometry. *Journal of Magnetic Resonance Series A*, 117, 94-97.

Sotiropoulos, S.N., Behrens, T.E., Jbabdi, S., 2012. Ball and rackets: Inferring fiber fanning from diffusion-weighted MRI. *Neuroimage* 60, 1412-1425.

Sotiropoulos, S.N., Moeller, S., Jbabdi, S., Xu, J., Andersson, J.L., Auerbach, E.J., Yacoub, E., Feinberg, D., Setsompop, K., Wald, L.L., Behrens, T.E., Ugurbil, K., Lenglet, C., 2013.

Effects of image reconstruction on fibre orientation mapping from multichannel diffusion MRI: Reducing the noise floor using SENSE. *Magn Reson Med*.

Starck, J.L., Pantin, E., Murtagh, F., 2002. Deconvolution in Astronomy: A Review. *Publications of the Astronomical Society of the Pacific* 114, 1051–1069.

Tax, C.M., Jeurissen, B., Vos, S.B., Viergever, M.A., Leemans, A., 2014. Recursive calibration of the fiber response function for spherical deconvolution of diffusion MRI data. *Neuroimage* 86, 67-80.

Tournier, J.-D., Calamante, F., Connelly, A., 2013. A Robust Spherical Deconvolution Method for the Analysis of Low SNR or Low Angular Resolution Diffusion Data, ISMRM 21st Annual Meeting, Salt Lake City, Utah, USA.

Tournier, J.D., Calamante, F., Connelly, A., 2007. Robust determination of the fibre orientation distribution in diffusion MRI: non-negativity constrained super-resolved spherical deconvolution. *Neuroimage* 35, 1459-1472.

Tournier, J.D., Calamante, F., Gadian, D.G., Connelly, A., 2004. Direct estimation of the fiber orientation density function from diffusion-weighted MRI data using spherical deconvolution. *Neuroimage* 23, 1176-1185.

Tournier, J.D., Yeh, C.H., Calamante, F., Cho, K.H., Connelly, A., Lin, C.P., 2008. Resolving crossing fibres using constrained spherical deconvolution: validation using diffusion-weighted imaging phantom data. *Neuroimage* 42, 617-625.

Tristan-Vega, A., Aja-Fernandez, S., Westin, C.F., 2012. Least squares for diffusion tensor estimation revisited: propagation of uncertainty with Rician and non-Rician signals. *Neuroimage* 59, 4032-4043.

Tristan-Vega, A., Westin, C.F., Aja-Fernandez, S., 2009. Estimation of fiber orientation probability density functions in high angular resolution diffusion imaging. *Neuroimage* 47, 638-650.

Tristan-Vega, A., Westin, C.F., Aja-Fernandez, S., 2010. A new methodology for the estimation of fiber populations in the white matter of the brain with the Funk-Radon transform. *Neuroimage* 49, 1301-1315.

Tuch, D.S., 2004. Q-ball imaging. *Magn Reson Med* 52, 1358-1372.

Tuch, D.S., Reese, T.G., Wiegell, M.R., Makris, N., Belliveau, J.W., Wedeen, V.J., 2002. High angular resolution diffusion imaging reveals intravoxel white matter fiber heterogeneity. *Magn Reson Med* 48, 577-582.

Wedeen, V.J., Hagmann, P., Tseng, W.Y., Reese, T.G., Weisskoff, R.M., 2005. Mapping complex tissue architecture with diffusion spectrum magnetic resonance imaging. *Magn Reson Med* 54, 1377-1386.

Wu, Y.C., Alexander, A.L., 2007. Hybrid diffusion imaging. *Neuroimage* 36, 617-629.

Yeh, F.C., Wedeen, V.J., Tseng, W.Y., 2010. Generalized q-sampling imaging. *IEEE Trans Med Imaging* 29, 1626-1635.